Thesis for the Degree of Doctor of Technology

Luminescence and mechanism studies of multi-colored phosphors with rare earth ions or transition metal ion

by

Lin Qin

Interdisciplinary Program of

Biomedical, Mechanical & Electrical Engineering

The Graduate School

Pukyong National University

August 2018

Luminescence and mechanism studies of multi-colored phosphors with rare earth ions or transition metal ion

희토류 이온과 전이금속 이온이 첨가된 다중색 형광체의 형광특성 연구

Advisor: Prof. Hyo Jin Seo

by

Lin Qin

A thesis submitted in partial fulfillment of the requirements for the degree of Doctor of Engineering in Interdisciplinary Program of Biomedical, Mechanical & Electrical Engineering, The Graduate School,

Pukyong National University

August 2018

Luminescence and mechanism studies of multi-colored phosphors with rare earth ions or transition metal ion

A dissertation

by

Lin Qin

Approved by:

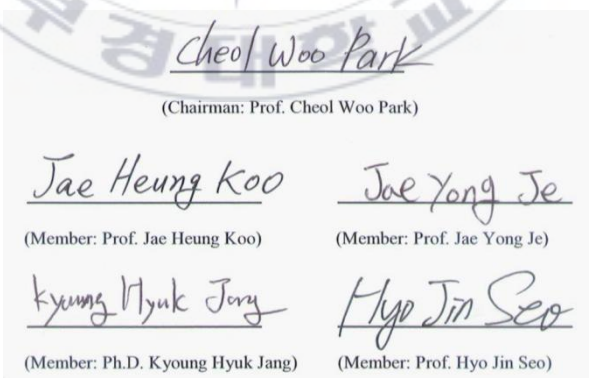

August 2018

Contents

Luminescence and mechanism studies of multi-colored phosphors with rare earth ions or transition metal ions

Lin Qin

Interdisciplinary Program of Biomedical, Mechanical & Electrical Engineering

Pukyong National University

Abstract

With growing global energy shortage and increasing environmental pressure, energy conservation and environmental protection has become one of the important subjects nowadays. In the field of general lighting, white LED products are attracting more and more attention for their advantages: lightning with high efficiency, long usage life, small size, low power and environmental protection, which is recognized as a new lighting source and would become the future trend of development. And as the most important components in white LEDs, phosphors have significant influence on its performance index: luminous efficiency, service life, color temperature and color rendering index. Generally, phosphors can be doped with rare earth (RE) ions for its special electronic structure, which has strong absorption ability, high conversion rate, strong emitting ability particularly in the visible region and the stable chemical

and physical properties. Among them, the most widely used methods to fabricate white LEDs are ultraviolet or near ultraviolet LEDs with tricolor phosphors (red, green, blue) combination, which has the best color and high fluorescent material luminous efficiency; The other is to combine blue LED with the yellow phosphor.

In the third chapter, Mn^{4+}-activated cubic phase Ba_5AlF_{13} red phosphors were prepared by the two-step coprecipitation method. The structural and optical features were conducted on the basis of X-ray diffraction (XRD), transmission electron microscopy (TEM), emission and excitation spectra, and luminescence decay curves. The $Ba_5AlF_{13}:Mn^{4+}$ phosphors can be efficiently excited by near-UV to blue light and exhibit the bright red emission at around 627 nm, which is assigned to the $^2E_g \rightarrow {}^4A_{2g}$ transition of the $3d^3$ electrons in $[MnF_6]$ octahedra. Temperature dependent emission spectra and decay curves from 10 to 550 K were introduced to deep understand the luminescence mechanism of Mn^{4+} in Ba_5AlF_{13} lattice. Notably, such a novel red phosphor shows excellent anti-thermal quenching behavior (~700% of emission intensity at 300 K relative to 10 K).

In the fourth chapter, $Ba_5Al_3F_{19}:Eu^{2+}$ blue-emitting phosphors were synthesized by the solid state reaction in a reductive atmosphere. The crystal structure of $Ba_5Al_3F_{19}:Eu^{2+}$ phosphors were characterized by using the X-ray powder diffraction (XRD) measurement. The luminescence properties are investigated systematically based on the crystal structure. Emission and excitation spectra of the $Ba_5Al_3F_{19}:Eu^{2+}$ phosphors along

with the decay curves were characterized. Under the excitation of UV light, the phosphor exhibits a broad band emission around 410 nm ascribed to the allowed $4f^6 5d \rightarrow 4f^7(^8S_{7/2})$ transition, together with a sharp line at 360 nm corresponding to the forbidden $4f^7(^6P_{7/2}) \rightarrow 4f^7(^8S_{7/2})$ transition of the Eu^{2+} ions. The temperature dependent emission spectra and decay curves were measured to investigate the origins of the emission and the thermal stabilities of the as-prepared phosphors. The as-prepared $Ba_5Al_3F_{19}:Eu^{2+}$ phosphors display interesting and stable luminescence properties, which can act as promising blue-emitting phosphor candidates.

In the fifth chapter, Series of Mn^{4+}-activated $LiLa_2NbO_6$ red emitting phosphors were prepared by the solid state method. The structural and luminescence properties are investigated on the basis of X-ray diffraction (XRD), emission and excitation spectra, and luminescence decay curves. The $LiLa_2NbO_6:Mn^{4+}$ phosphors can be efficiently excited by near-UV to blue light and exhibit bright red emission at around 712 nm, which is assigned to the $^2E_g \rightarrow {}^4A_{2g}$ transition of the $3d^3$ electrons in $[MnO_6]$ octahedra. Temperature dependent emission spectra and decay curves from 10 to 480 K are analyzed to understand the luminescence mechanism of Mn^{4+} in $LiLa_2NbO_6$ lattice. Notably, such a novel red emitting phosphors shows special anti-thermal quenching behavior.

1. Introduction

1.1. Introduction to W-LEDs

As a new generation of solid-state lighting source, white light-emitting diodes (W-LEDs) as new type of high efficient lighting source since 1990s absorb much attention due to several advantages, such as the environmental protection and energy saving, small volume, long service life, high luminous efficiency and so on.[1][2] W-LED is a kind of semiconductor diode with diode characteristics which can transfer electric energy into light energy through electronic devices. The principle and common semiconductor light-emitting diode were shown in **Fig. 1-1**.[3]

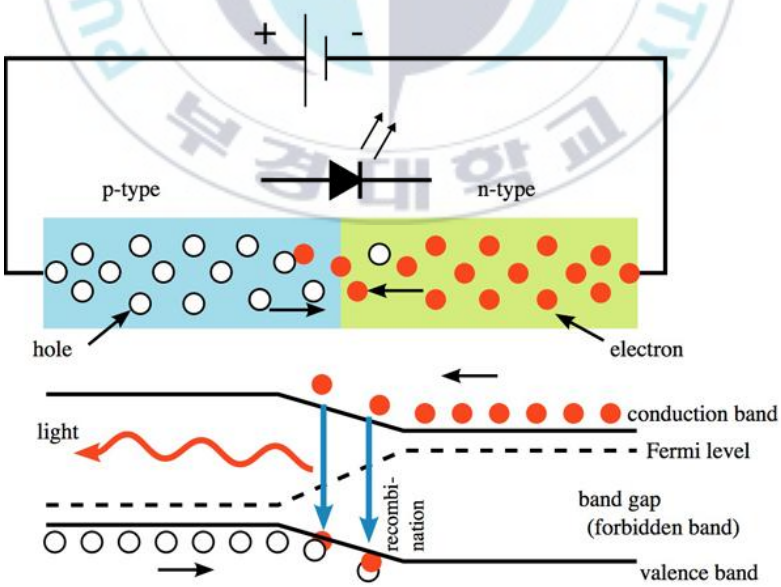

Fig. 1-1 Luminescent mechanism of LED.

Under the condition of the external power supply, the internal structure will be separated into the p and n regions which are similar to the semiconductor diode, and in the intersecting interface, PN junction can be formed. LED luminescence usually consists of carrier injection, composite radiation, and light energy transmission under forward bias. Due to the different materials with different bandgap, they always emit different colors of light. Generally, the current of LED can be controlled by the voltage, which is of great significance in terms of economic value, market application prospect and social benefit.

1.1.1. Technical scheme of W-LEDs

The first commercial W-LEDs were produced by the Japanese Company Nichia, and since then the investigation of W-LEDs absorbs more attention. In general, there are three ways to produce W-LEDs.[4][5] Firstly, YAG:Ce^{3+} yellow phosphor is excited by the blue light LED chip, which produces yellow light, and then produces white light with residual blue light; Secondly, red, green and blue LED chips are used to assemble the light source of W-LEDs; Thirdly, use ultraviolet or deep ultraviolet LED chips to excite red, green and blue phosphors, and finally compound to white light. Among them, the first one is the mainstream of the current preparation of white PC - LED method. However, it also has the following deficiencies: the lack of red light and green light composition in the spectrum, which will leading to the final white LED with high color temperature (the color temperature, Tc), low color rendering index (the

color - rendering index, Ra).[6] The drawback of the second way is the purity in color of the obtained white LED, it is difficult to control the ratio of the red, green and blue LED chips. In addition, the luminous efficiency is low. According to the third way, ultraviolet or near ultraviolet LED chips can effectively excite the trichromatic phosphors, with high color rendering. The color temperature can be matched in the range of 2500 ~ 10000 K. Therefore, in order to improve the luminescence efficiency, color temperature, service life, color index and other performance indexes of this kind of LED, the key is to develop a new type of red, green and blue phosphors.

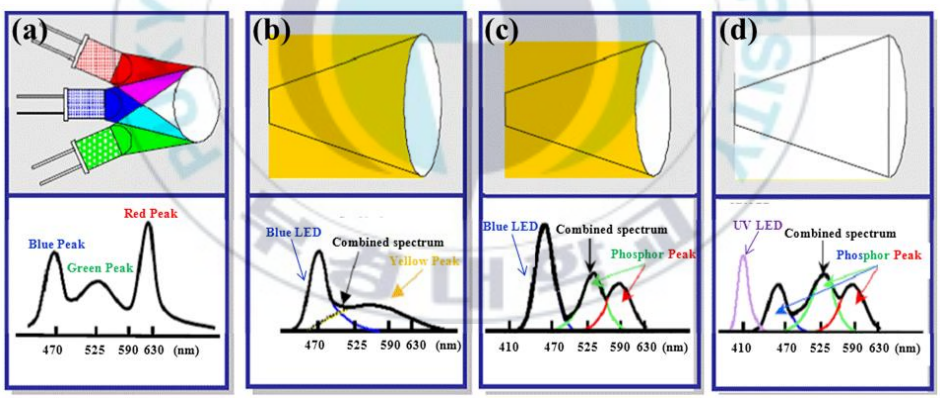

Fig. 1-2 Technical scheme of white LED

In this chapter, the luminescence principle and research status of rare earth or transition metal luminescent materials were summarized. The advantages and research status of luminescent materials of different

matrix were introduced. Accordingly, the starting point of this thesis is shown as follows: the rare earth ions or transition metal ions doped with different substrate materials were prepared using traditional high temperature solid state method or two steps co-precipitation method, the luminescence performance and luminescence mechanism were deeply investigated to find new field of vision for their applications.

1.1.2. Characteristics of W-LEDs

Compared with traditional lighting technology, W-LEDs lighting technology has many advantages:[7]

(1) Energy conservation and environmental protection: W-LEDs with low energy consumption and high luminous efficiency are novel energy-saving lighting source. In addition, the currently widely used energy-saving lamps, which contain the chemical mercury Hg in the pollution environment, are harmful to the environment and human health. However, during the process of production and use of the W-LEDs, no harmful chemical substances to the environment or human health will be produced, which eliminate the pollution of mercury Hg on the human body and the surrounding environment. So W-LED also called as a kind of "green" lighting equipment;

(2) Wide spectral range: the emission spectrum of W-LED light source can cover the entire visible area;

(3) High safety performance: The working voltage of W-LED is low,

heating process is slow, no frequency flashing, no ultraviolet and infrared radiation;

(4) Long lifetimes: W-LED can live up to ten thousands hours, which is the longest living light source;

(5) Small size and firmness: W-LED is easy to design with exquisite appearance fixed by epoxy resin with good physical and chemical stability, and W-LED can withstand certain mechanical forces. At the same time, due to the exquisite design, W-LED can be used for simple plane packaging and complex stereo lighting system;

(6) The color temperature, brightness of W-LED almost close to fluorescent lamp, but with faster reaction rate.

1.1.3. Growing trend of W-LEDs

In recent years, there has been an increasing trend for white light emitting diodes (W-LEDs) to replace the conventional incandescent and fluorescent lamps, due to their long lifetime, high energy efficiency, environmental protection and so on. At present, commercial W-LEDs are fabricated by combining one or two different types of phosphors that can be excited by the blue LED chip.[8] However, white LED with yellow YAG:Ce phosphor excited by blue GaN has the following problems: white emitting color changes with input power, the mix-up of the two colors results in low color rendering index and strong dependence of white color quality on an amount of phosphor leads to low reproducibility.[9][10] In order to overcome

these problems, it is essential to explore novel and efficient full-color luminescent materials that can directly emit white light under the excitation from the ultraviolet LED chip.[11] Recently, a lot of attention has been paid to single-phased white light emitting phosphors,[12] which have a large potential application for white light LED. In these systems, the performance of white LEDs, including the CRI, color temperature, and color range, will significantly depend on the employed phosphors.[13]

Recently, Bridgelux announced that the luminous efficiency of its white LEDs would be significantly improved, with the highest luminous efficiency of warm white LEDs up to 160 lm/W(color temperature 3000 K, color index 80). In addition, more than 10% more energy can be saved with high efficient. Facing several challenges of white-light LED, the development trend can be summarized as follows:

(1) Reduce the production cost of white LED: at present, the price of white LED sold in the market is very high, which result in the disadvantage in the lighting market. Hence, a major obstacle to its application and development is the high price of white LED. Therefore, in the future, the production cost and the reduction of the cost of the white LED must be controlled.

(2) The improvement of the luminous efficiency of white LED: at present, the luminous efficiency of the commercialized white LED is generally lower, 50 lm/W, which cannot met the minimum efficiency requirement by standard fluorescent lamps. At present, in order to

improve the efficiency of quantum efficiency, optimize LED packaging process and improve lamp design were carried out. The improvement of the luminous efficiency of white LED will further promote the application of white LED lighting technology.

(3) Improve the color purity of white LED. The commercial white LED shows index is about 75 and the color temperature is over 5000 K, which is difficult to meet the requirement of high quality lighting. In addition, the spectral range of white LED is as far as possible to match the spectrum of sunlight, which is an important development direction for white LED.

1.2. Solid luminescence theory

Usually, except for the thermal radiation, the luminescence of inorganic materials is composed of the following processes:[14] (1) absorption or excitation, (2) energy transfer process, and (3) emission. Most luminescent materials consist of a so-called host lattice and single or several termed activators. In this case, the host lattice plays two distinct roles: as a passive matrix, which only provide spatial locations of the activator ions; and as an active matrix, which will participant in the luminescence process, exerting its own specific luminescent properties influence on the spectroscopic behavior of the activator.

Luminous process as shown in **Fig. 1-3**, assuming that the absorption of lattice matrix M does not produce radiation, A (the activator), S

(sensitizer) are for doping ions. The lattice M absorbs excitation energy firstly, and then passes to the excited state, finally it returns to the ground state. Here, there will be three ways: firstly, in the form of radiation release, called emission; Secondly, the energy is released into the adjacent lattice in the form of heat, called thermal quenching; Thirdly, the doped ion S absorbs energy, and the passes all or part of the energy to A and emits light. A is the activator, and S is the sensitizer of A.[15]

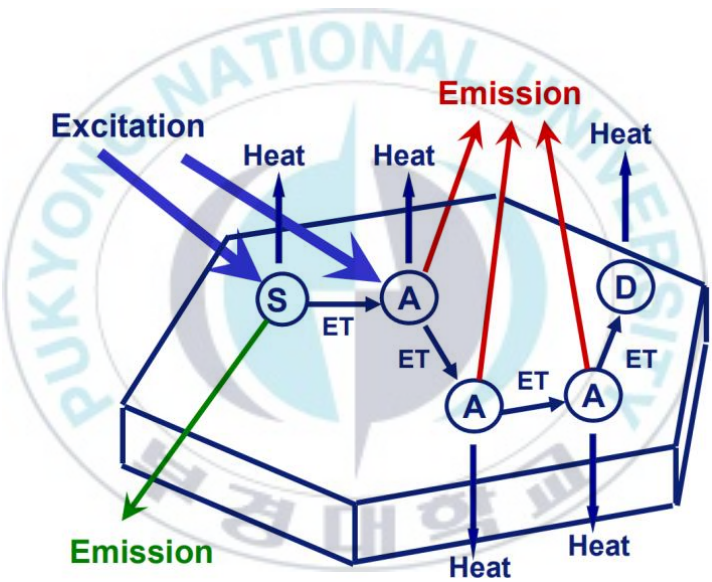

Fig. 1-3 Physical process of solid luminescence

1.3. Rare-earth luminescence

Rare-earth elements are composed by seventeen chemical elements in the periodic table, specifically the fifteen lanthanides: lanthanum (La),

cerium (Ce), praseodymium (Pr), neodymium (Nd), promethium (Pm), samarium (Sm), europium (Eu), gadolinium (Gd), terbium (Tb), dysprosium (Dy), holmium (Ho), erbium (Er), thulium (Tm), ytterbium (Yb), lutetium (Lu), as well as scandium (Sc) and yttrium (Y).[16] In 1794, rare earth ions were firstly found from the yttrium silicon beryllium by a famous chemist Duo Lin from Finland. The chemical and physical properties of these rare earth ions are very similar with each other with rich outer levels. Rare earth ions with large radius show strong polarization force, active chemical characteristics. However, rare earth elements usually found in extremely complex mines, and separation is more difficult. Until now, rare earth metal ions are the most widely used as activator ions in luminescent materials.

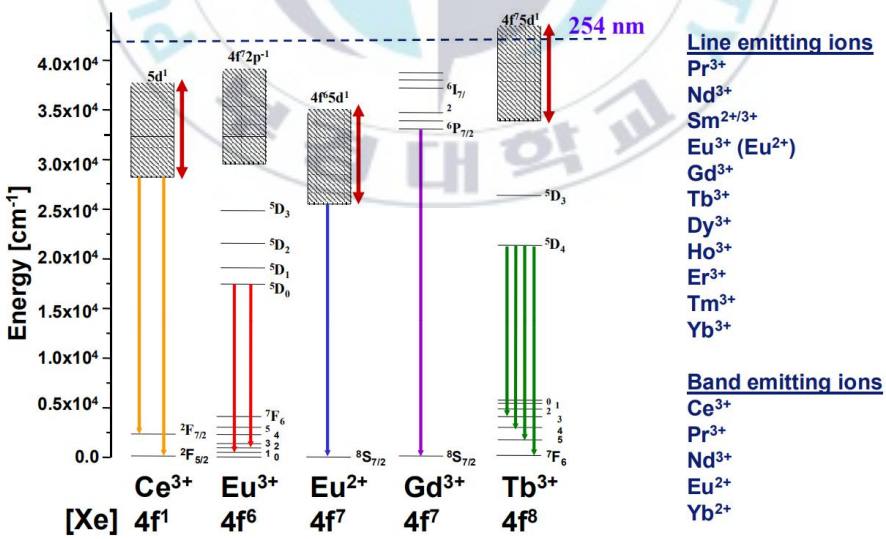

Fig. 1-4 Simplified energy level schemes of selected RE ions.

The electronic configuration of rare earth elements is [Xe]$6s^2 5d^1 4f^n$. In

ionization state, the electrons from the layers 6s and 5d are lost, leading to the electronic configuration as [Xe]$4f^n$ for the trivalent rare earth elements, like La^{3+}, Eu^{3+}, Gd^{3+} and so on. Depending on the atomic number, the 4*f* orbitals are more or less filled, the electron number varying from 0 (La^{3+} or Ce^{4+}) to 14 (Lu^{3+}). For the rare earth elements, two different orbitals are usually involved in electronic transitions.

1.3.1. The rare earth ions with 4*f*-4*f* transitions

The rare earth ions with 4*f*-4*f* transitions include Eu^{3+}, Sm^{3+}, Tb^{3+} and so on. The unpaired electrons in the 4*f* orbitals are the origins of the very special electronic and magnetic properties of the rare earths. The 4*f*-4*f* transitions are also called “internal” transition, since 4*f* orbitals are shielded from the surroundings by the full filled $5s^2$ and $5p^6$ orbitals, which have wider radial expansion.[17]

The main optical properties associated with 4*f*-4*f* transitions can be described as follows:

(1) 4*f*-4*f* transitions usually consist of sharp peaks because the 4*f* orbitals lie inside and shielded from the surroundings by the full filled $5s^2$ and $5p^6$ orbitals. In other words, the coupling with phonons (vibrations of the matrix) is very low.

(2) The energy (or wavelength) of a particular 4*f*-4*f* transition of a given rare earth is equivalent even different host matrix, only their intensities change. This fact is also due to the small effect of the crystal field of

the matrix on the 4*f* energy level positioning.

(3) Due to the selection rules (Laporte's rules, DE transitions are forbidden), the intensities of 4*f*-4*f* transitions are usually very low. Nevertheless, the forced DE transitions are enough to give intense emissions, for example Eu^{3+} or Tb^{3+}, which usually act as famous activators in commercial phosphors).

(4) Due to the huge number of energy levels in 4*f* orbitals, most of rare earth ions show rich electronic transitions between 4*f* levels. However, it is unfavorable for emission properties due to a poor chromatic quality and a reduced quantum yield. As a consequence, only few and selected 4*f*-4*f* transitions are used in practical cases, for example, Eu^{3+} ($^5D_0 \rightarrow {}^7F_J$) act as a red emitter, Tb^{3+} ($^5D_4 \rightarrow {}^7F_J$) act as a green emitter, Gd^{3+} ($^6P_J \rightarrow {}^8S_{7/2}$) act as a UV emitter.

1.3.2. The rare earth ions with 4*f*-5*d* transitions

The rare earth ions with 4*f*-5*d* transition include Ce^{3+}, Eu^{2+} and so on. In terms of energy, 5*d* levels are above the 4*f* fundamental level. The energy position corresponding to the five 5d orbitals are external and strongly impacted by the crystal field and the symmetry of the host lattice.[18]

The main properties of 4*f*-5*d* transitions are described compactly as follows:

(1) The absorption or emission spectra of 4*f*-5*d* transitions always consist of broad band. Contrary to the 4*f*-4*f* transitions, the crystal field (5d

orbitals) is strong. The coupling with phonons is high.

(2) The energy (or wavelength) of the 4*f*-5*d* transition are strongly dependent on the host lattice. For example, the emission from Eu^{2+} with 4*f*-5*d* transitions occur from the UV to red region.

(3) Contrary to the 4*f*-4*f* transitions, the intensities of the 4*f*-5*d* transition are very high (ED transitions allowed).

(4) For most rare earth ions, the 4*f*-5*d* transitions are too energetic to be used in classical applications. For trivalent lanthanides, only Tb^{3+}, Ce^{3+} and Pr^{3+} are practically having 4*f*-5*d* absorption transitions close to the visible range (> 200 nm in wavelength). On the contrary, the energies of the 5*d* bands are quite low for the divalent lanthanides. The lowest ones are found with Eu^{2+} and Ce^{3+}. As a consequence, Eu^{2+} and Ce^{3+} ions have been mostly studied due to their absorption and emissions in the UV-visible wavelengths.

1.4. Transition metal luminescence

The study of the physics and chemistry properties of the transition metal coordination compounds has developed rapidly through photochemistry, absorption and reflectance spectroscopy, and emission spectroscopy.

1.4.1. The transition metal ions (d^n)

Transition metal ions have an incompletely filled *d* shell (d^n $0<n<10$).

the energy levels originating from such a configuration haven been calculated by Tanabe and Sugano, taking the mutual interaction between the *d* electrons as well as the crystal field strength into account. **Fig. 1-5** shows the typical results for the configurations d^2, d^3, d^4,d^5, d^6, d^8.

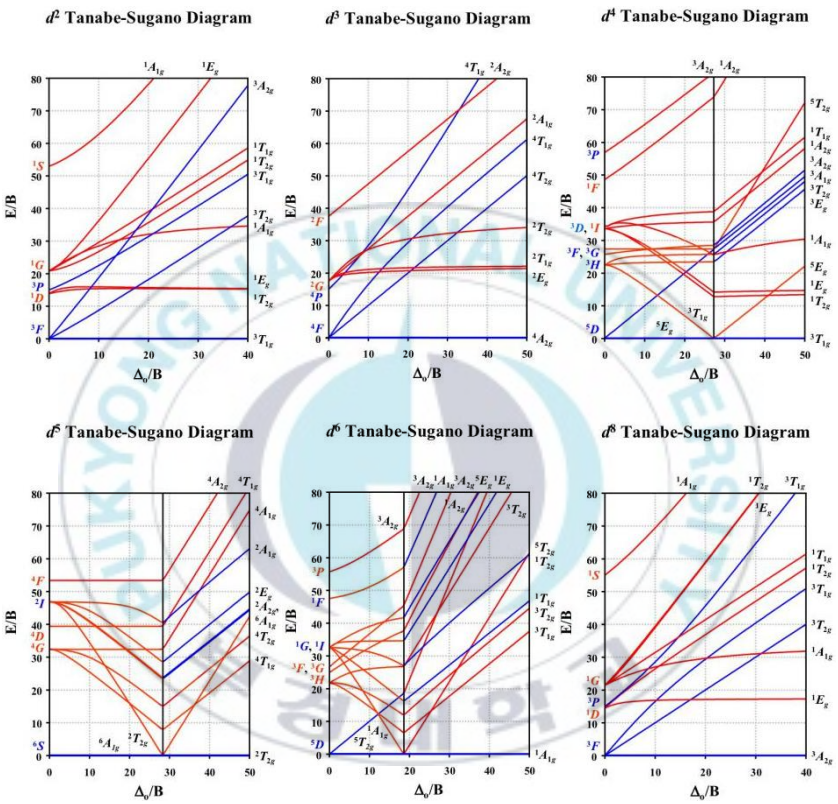

Fig. 1-5 Tanabe-Sugano diagrams for an ideal octahedral transition metal complex with d^2, d^3, d^4,d^5, d^6, d^8 configurations.

1.4.2. The transition metal ions (d^0)

Here, we wish to describe new developments refer to central highly-charged transition metal ion without d electrons surrounded by a

number of oxygen ions (usually 4 or 6 in a tetrahedral or octahedral arrangement, respectively). Compounds like $CaWO_4$, $YNbO_4$, YVO_4 are the best-known examples and have been studied extensively. The absorption spectra show strong and broad bands in the ultraviolet region due to the charge transfer transitions from oxygen to the d^0 orbitals.

The luminescence of $CaWO_4$ has been known for a long time. This phosphor finds application since many decades (nowadays only as an X-ray phosphor in intensifying screens). As a luminescent mineral (scheelite), this compound has also been known to mineralogists. The luminescence which can be excited by short-wavelength ultraviolet radiation, X-rays, cathode rays etc., shows an emission spectrum consisting of a very broad band peaking at about 420 nm). This emission band corresponds to a broad excitation band peaking at about 240 nm, so that the Stokes shift of this luminescence is very large (some 16000 cm^{-1}).[19]

Usually, the spectra position of this absorption transition depends on many factors: the ionization potential of $d^1 \rightarrow d^0$ ionization, the number and nature of the ligands, and the interaction between ions mutually in the lattice.

1.5. Progress in the study of white LED phosphors

The use of phosphors by human probably started more than 2000 years ago when they were used in fireworks to modify the color output, but real phosphor development is a 20th century phenomena starting in the 1940s,

and its more recent development has most of the market demand being generated by cathode ray tubes (TVs, PC monitors, test equipment) and fluorescent lighting. However, during the last five years white LEDs have become very important lighting sources and the importance of LED phosphors for white and coloured light generation must be considered an important market driver in the future, and perhaps unfortunately, as a disruptive technology.[20]

1.5.1. Luminescence system with activator Eu^{3+}

Eu^{3+}, one of the rare earth ions is a typical red glow ion, luminous mainly comes from the 4*f* layer transition between energy levels in a sharp line, its luminescent properties and has the close relationship between material structure, the realization of its glow from the upper level 5D can realize electronic moved to the next level of 7F, as shown in **Fig. 1-6**.As a result of the nondegenerate $^5D_0$ level to the multiplet F_J (J = 0, 1, 2, 3, 4) level transition spectral line number, can reflect $7F_J$ (J = 0, 1, 2, 3, 4) of the crystal field splitting, so it can be used to explore the local structure of rare earth ions.[21] In particular, when the Eu^{3+} occupies an asymmetric central position in the matrix, its $^5D_0$-$^7F_2$ transition has a strong emission in the red range, so Eu^{3+} ion is an ideal red phosphor activator.

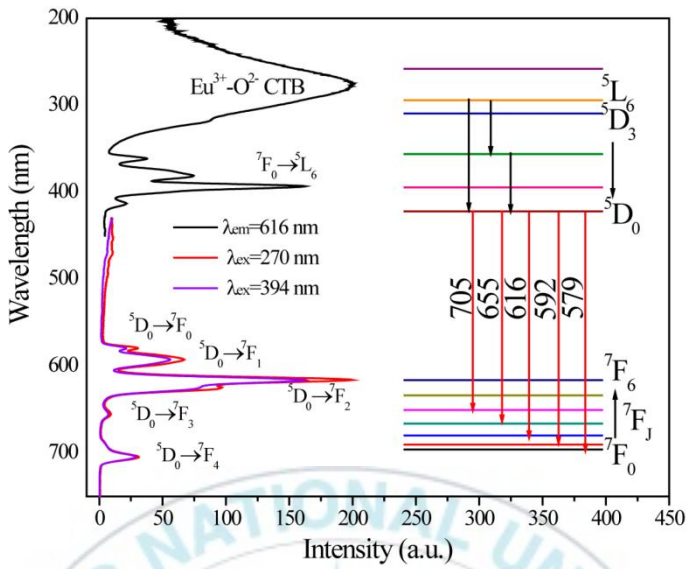

Fig. 1-6 typical energy level diagram for excitation and emission transitions of Eu^{3+}.

Cubic Y_2O_3:Eu^{3+} is one of the most important commercial red phosphors used in lighting, plasma display panel (PDP), field emission display (FED), thermal calibration, etc. Phosphors of lower particle size with higher luminescence efficiency are the most desired materials for use in compact fluorescent lamps of higher lumen power and display panels of better image-resolution.[22]

1.5.2. Luminescence system with activator Eu^{2+}

The luminescence properties of Eu^{2+} ion with the 4*f*-5*d* transition are sensitive to the crystal field and covalency. Usually, the Eu^{2+} doped phosphors have a strong absorption in the UV to the visible spectral

region and exhibit broad band emissions covering the color from blue to red. The 5*d* levels of Eu^{2+} ions are not shielded completely by the outer environment which will split under various ligand field strength, and the number of split levels is determined by the local symmetry around the Eu^{2+} ions. The 5*d* orbitals of Eu^{2+} are inclined to be separated as T_2 and E levels. In such a model, the energy transfer process will occur between the ground state ($^8S_{7/2}$) and the split T_2 and E levels.

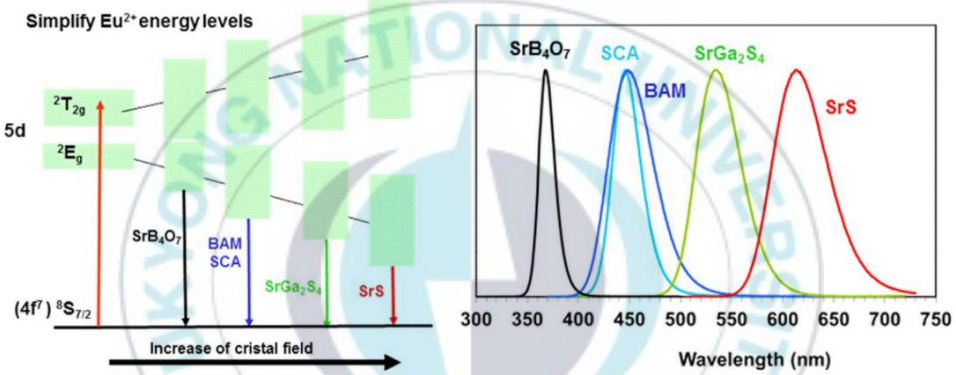

Fig. 1-7 Schematic splitting of the Eu^{2+} 5*d* levels in several host matrixes and the associated emission spectra (obtained under UV excitation).

$CaAlSiN_3:Eu^{2+}$ red phosphors were prepared by the self-propagating high-temperature synthesis and their luminescent properties were deeply investigated by Piao.[23] The obtained red phosphors show low-temperature quenching effect, as well as excellent chemical and thermal stabilities. And such an efficient phosphor can be used as a potential candidate for the phosphor-converted white LEDs.

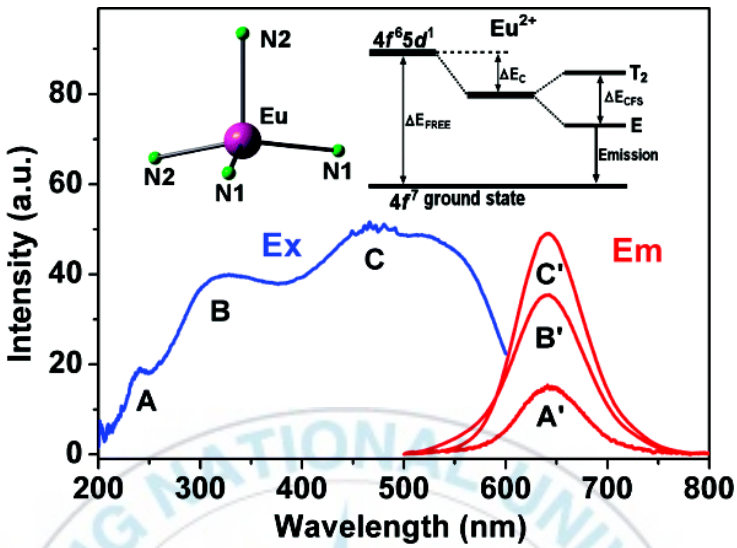

Fig. 1-8 Typical photoluminescence excitation (λ_{em} = 649 nm) and emission spectra of $Ca_{0.98}Eu_{0.02}AlSiN_3$ under different excitation wavelength and the schematic picture of the influence of the environment of a Eu^{2+} on the positions of electronic states.

The new narrow-band red-emitting phosphor material $Sr_4[LiAl_{11}N_{14}]:Eu^{2+}$ was synthesized by solid-state reaction using a tungsten crucible with a cover plate in a tube furnace. When excited with blue light (460 nm), it exhibits red fluorescence with an emission maximum at 670 nm and a full width at half-maximum of 85 nm.[24]

1.5.3. Luminescence system with activator Ce^{3+}

Ce^{3+} ion with its single *f*-electron in the 4*f* shell is an excellent system

to study behavior of the one-electron 4*f* and 5*d* states in different environment. Such a simple electronic configuration leads to a simple energy level scheme, which for the free trivalent cerium ion is as follows: one term ^2F in the $4f^1$ configuration (which is split by spin-orbit interaction into the $^2F_{5/2}$ and $^2F_{7/2}$ states separated by about 2000 cm^{-1}) and one term ^2D in the $5d^1$ configuration (which can be split into the $^2D_{3/2}$ and $^2D_{5/2}$ states). The energy gap between the $^2F_{5/2}$ and $^2D_{3/2}$ states of a free Ce^{3+} ion is 49,737 cm^{-1}.[25][26] In crystals, however, the ^2D state is lowered down to about 30,000-35,000 cm^{-1}.[27] Since the 5d states strongly interact with crystal lattice, the 4*f*-5*d* absorption and 5*d*-4*f* emission is essentially host-dependent. In this way, it is interesting and important to analyze the main spectral features of these transitions in different hosts and estimate basic parameters of crystal field splitting and electron-vibrational interaction (EVI) of the 5d electron states of trivalent cerium with crystal lattice environment.

The 4*f*-5*d* excitation and 5*d*-4*f* emission spectra of Ce^{3+} in various compounds have been extensively studied in the last years. The main yellow phosphor, $Y_3Al_5O_{12}:Ce^{3+}$ (YAG:Ce), was reported in 1967 with its primary use (prior to pcLEDs) in CRTs. In pcLEDs, YAG:Ce absorbs blue LED radiation through the allowed $4f^1 \rightarrow 5d^1$ transition and emits yellow light via the reverse $5d^1 \rightarrow 4f^1$ transition (**Fig. 1-7**). The emission from the lowest excited $5d^1$ level is to the spin-orbit split $4f^1$ ground states, leading to an extremely broad emission band with a FWHM > 100 nm.,[28] The absorption and emission transitions belongs to YAG:Ce are parity and spin

allowed, giving strong absorption of blue LEDs and a fast decay time that prevents saturation quenching. The quantum efficiency (QE) of YAG:Ce under blue LED excitation is >85%, even at 200 ^{o}C.[29]

1.5.4. Luminescence system with activator Mn^{4+}

Recently, more attention has been paid to red phosphors doped with transition metal Mn^{4+} ions. The optical properties of Mn^{4+} are closely related to the host matrix.[30] Generally, Mn^{4+} ions can only be accommodated and stabilized in an octahedral lattice site of the host crystals, with broad absorption spectrum in the range of 220 - 600 nm and show red-emitting within the range 600 - 780 nm.[31]

The energy levels of the Mn^{4+} ($3d^3$) ions in a crystal could split into a number of sublevels depending on the crystal-field strength and symmetry. The splitting of the energy levels of Mn^{4+} in an octahedral crystal field can be described by the Tanabe-Sugano diagram of the d^3 electronic configuration,[32] as displayed in **Fig. 1-6**.

As previously reported, Mn^{4+}-doped luminescence materials can be divided into two categories: Mn^{4+}-doped fluorides and Mn^{4+}-doped oxides. For example, highly efficient non-rare-earth red emitting phosphors, such as $K_2TiF_6:Mn^{4+}$, $K_2SiF_6:Mn^{4+}$, $NaGdF_4:Mn^{4+}$ and $NaYF_4:Mn^{4+}$, were prepared by cation exchange approach for warm white light-emitting diodes. Among these obtained red phosphors, $K_2TiF_6:Mn^{4+}$ red phosphor show photoluminescence quantum yield as high as 98%, as shown in **Fig.**

1-7. [33]

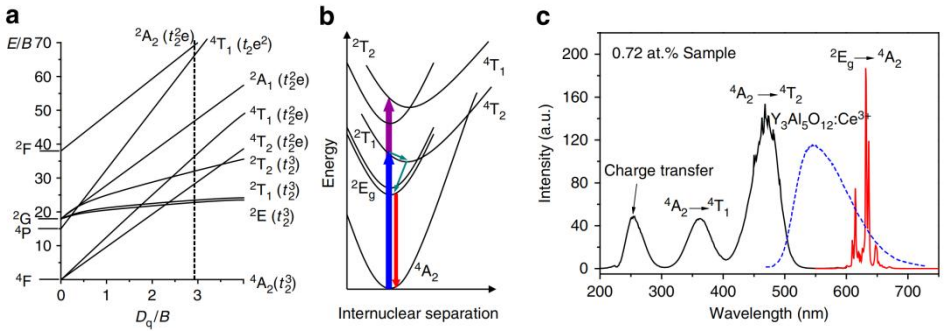

Fig. 1-9 Energy levels and optical spectra of Mn^{4+} emitters in fluoride phosphors. (a) Tanabe-Sugano energy diagram of a $3d^3$ system in an octahedral crystal field. (b) Configurational coordinate diagram for Mn^{4+} ions in fluoride hosts. (c) Room temperature excitation and emission spectra of the $K_2TiF_6:Mn^{4+}$ (0.72 at.%) sample. The dashed line displays the emission spectrum of commercial $Y_3Al_5O_{12}:Ce^{3+}$ yellow phosphor.

The luminescent properities of Mn^{4+} ions doped $MAl_{12}O_{19}$ (M=Ca, Sr, Ba) were studied by Kang.[34] Mn^{4+} actived $CaAl_{12}O_{19}$ and $SrAl_{12}O_{19}$ phosphors exhibit red emission around 658 nm due to the $^2E \rightarrow {}^4A_2$ transition of Mn^{4+} ions with high thermal stability.

1.5.5. Luminescence system with activator Mn^{2+}

Mn^{2+}, a transition metal center, has been doped into many inorganic hosts used as luminescent centers with colorful emission ranging from 490 to 750 nm. From the Tanabe-Sugano diagrams, it can be deduced that the

Mn^{2+} ions can be excited in several bands in the 400 - 520 nm range related to the $^6A1 \rightarrow {}^4A_1$, ^4E, $^6A_1 \rightarrow {}^4T_1$ and $^6A_1 \rightarrow {}^4T_2$ transitions. The emission wavelength position of the Mn^{2+} ion depends strongly on the host lattice, including the strength of the ligand field and the coordination number (CN).[35] Generally, Mn^{2+} ion usually gives a green to yellow emission when located on a lattice with tetrahedrally coordinated Mn^{2+} (weak crystal-field) site, whereas it shows an orange to deep red emission with octohedrally coordinated Mn^{2+} (strong crystal-field) site.[36]

Great efforts to investigate the Mn^{2+} single doped compounds have been made and some Mn^{2+} doped phosphors with very good luminescence properties have been synthesized successfully.[37][38] For example, Wu et al.[39] reported the photo-luminescence of single Mn^{2+} doped $KMgBO_3$ red phosphors.[40] Duan[41] reported that Mn^{2+}-activated CaZnOS shows great potential for application as an alternative red-emitting LED conversion phosphor due to its high absorption and strong excitation bands.[42]

1.5.6. Study conclusion and adaptation prospect

With the continuous study of luminescent materials, more and more luminescent materials are presented; however, the luminescent performance cannot meet the requirements of commercial white leds. Therefore, the luminescent materials should be developed in the direction of high efficiency, high stability and high color purity. The specific improvement plan is as follows:[43][44]

1. Improve the preparation methods (solid phase method, precipitation method, hydrothermal method, spray pyrolysis method) to reduce the preparation cost, at the same time, develop a new type preparation plan (sol-gel method, gas phase chemical method, microwave method, ultrasonic method) for synthesis nano-sized phosphors to improve luminescence properties.
2. Developed a new type of high efficiency activator: most of the red light emitting materials used by the activator for rare earth metal ions due to the electronic structure with complex and rich transition levels. Select the appropriate ions as activator has become a major breakthrough in recent years.
3. Improve the formulation of traditional phosphor through doping of other ions, adding fluxing agent, etc., to improve the luminous efficiency of white LED.

1.6. Starting point and research content

1.6.1. Starting point

This topic mainly choose fluorides as lattices, compared with the oxygen-based matrix have some comparative advantages as matrices for lower phonon energy, high refractive index, high quantum efficiency, and high chemical and mechanical properties. This could significantly improve the thermal stability from the viewpoint of reducing the thermal quenching of the excited states of the activator ions.[45][46] Therefore, development of

high efficiency of white LED phosphor with fluoride lattice is necessary.

Luminescence of divalent rare earth europium ion Eu^{2+} is mainly due to electron transitions between the 4*f* layer and 5*d* layer, and the luminescence performance is closely related to the structure of the material. Eu^{2+} is often used as an efficient blue emission activator ion in most matrix lattices. In addition, Mn^{4+} ion, as a transition metal ion with an unfilled $3d^3$ electron shell, plays an important role in lighting and display fields. Contrary to the rare-earth-ions with the parity-forbidden *f-f* transition, the luminescence properties of Mn^{4+} with the *d-d* transition are easily influenced by various coordinated environmental factors.

Based on the above consideration, this thesis will use the high temperature solid instead should method and the two step coprecipitation method to prepare several red and blue luminescent materials, and test their morphology, excitation spectra, emission spectra and decay curves to deeply study the potential applications.

1.6.2. Research content

The specific research contents are as follows:

1. Prepare the samples, $Ba_5AlF_{13}:Mn^{4+}$ red phosphors, by the two-step coprecipitation method. Prepare the samples, $Ba_5Al_3F_{19}:Eu^{2+}$ blue phosphors and $LiLa_2NbO_6:Mn^{4+}$ red phosphors, by the solid state reaction. And the $Ba_5Al_3F_{19}:Eu^{2+}$ blue phosphors were prepared in a reductive atmosphere.

2. X-ray diffraction (XRD) measurements were carried out to determine the composition of materials, and determine the presence of impurities by comparing with standard PDF card. And the transmission electron microscopy (TEM) was carried out to confirm the morphologies of the obtained phosphors.

3. The excitation, emission spectroscopy and decay curves were measured to analyze the luminescence performance of the obtained phosphors.

4. The thermal stability of the phosphor powder was tested to value their potential applications, and compared the obtained performance parameter with other reported phosphors..

2. Preparation and spectroscopic measurement

2.1. Experimental material

The name, purity and supplier of the drug used in this experiment are shown in **table 2-1**.

Table 2-1 List of chemical reagents

number	reagent	purity	Company
1	$KMNO_4$	Analytical	Sigma Adrich
2	KF	Analytical	Sigma Adrich
3	HF	Analytical	Sigma Adrich
4	$Ba(NO_3)_3$	Analytical	Sigma Adrich
5	$Al(NO_3)_3$	Analytical	Sigma Adrich
6	NaF	Analytical	Sigma Adrich
7	H_2O_2	Analytical	Sigma Adrich
8	NaOH	Analytical	Sigma Adrich
9	BaF_2	Analytical	Sigma Adrich
10	AlF_3	Analytical	Sigma Adrich
11	EuF_3	Analytical	Sigma Adrich
12	Li_2CO_3	Analytical	Sigma Adrich
13	La_2O_3	Analytical	Sigma Adrich
14	MnO_2	Analytical	Sigma Adrich
15	Nb_2O_5	Analytical	Sigma Adrich

2.2. Laboratory apparatus

In this experiment, the experimental equipment used during the synthesis process is shown in **table 2-2**.

Table 2-2 Instrument List

number	experimental equipment
1	Electronic scales
2	Agate mortar and agate grinding bar
3	Beaker and glass rod
4	Magnetic heating agitator and magnetic rotor
5	Electric hot air drying oven
6	Al_2O_3 Crucible and crucible forceps
7	High temperature box type resistance furnace (0-1600 ^oC)

2.3. Sample preparation

2.3.1. Synthesis process of $Ba_5AlF_{13}:Mn^{4+}$ nanoparticles

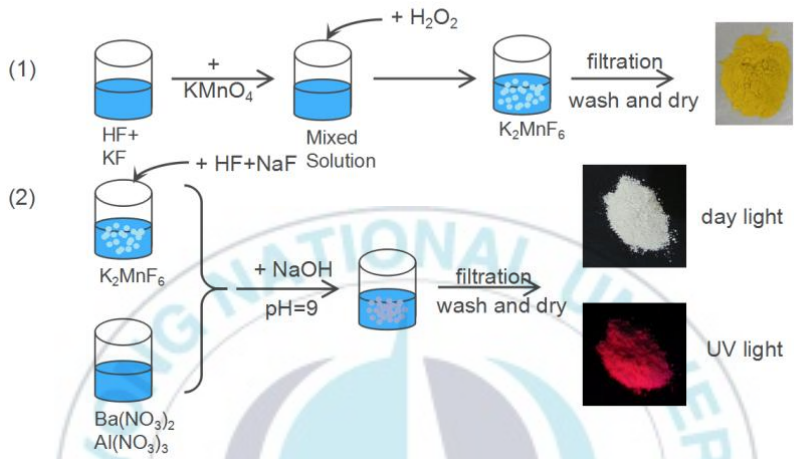

Fig. 2-1 Two-step synthesis of the $Ba_5AlF_{13}:Mn^{4+}$ nanoparticles

The $Ba_5AlF_{13}:Mn^{4+}$ nanoparticles were prepared via the two-step coprecipitation method as shown in **Fig. 2-1**. The chemical reagents in the synthesis process were $KMnO_4$, KF, HF, $Ba(NO_3)_2$, $Al(NO_3)_3$, NaF, H_2O_2, and NaOH. Firstly, the tetravalent manganese source K_2MnF_6 was synthesized according to the Bode's method.[47] The starting materials KF and $KMnO_4$ were both dissolved in HF solution. The mixed solution was stirred at least 30 min and then doped with H_2O_2 aqueous solution drop by drop until the yellow precipitate K_2MnF_6 obtained. In the process of preparing the $Ba_5AlF_{13}:Mn^{4+}$ nanoparticles, K_2MnF_6 was added to the HF

solution, and then double molar amount of NaF was added to the solution **A**.

In separate solution, $Ba(NO_3)_2$ and $Al(NO_3)_3$ were both dissolved in water solution **B**. Afterward, mixed **A** and **B** solutions and an appropriate amount of NaOH were added drop-wise under stirring the solution to adjust the pH value to about 9. Finally, the resulting white slurry was filtered, washed for several times using distilled water and then dried at 180 °C for 5 h.

2.3.2. Synthesis process of $Ba_5Al_3F_{19}:Eu^{2+}$ phosphors

The preparation of $Ba_{5(1-x)}Al_3F_{19}:5xEu^{2+}$ phosphors (x=0.001 - 0.04) were carried out by using the traditional solid-state reaction. The raw materials were analytically pure BaF_2, AlF_3 and EuF_3 from commercial sources. The $Ba_5Al_3F_{19}:Eu^{2+}$ phosphors were obtained by heating stoichiometric mixture of 5:3=BaF_2/AlF_3 at 800 ^oC for 2 hours in a reducing atmosphere according to the reference.[48] The doping level of Eu^{2+} ions were ranging from 0.1 to 4.0 mol% substituted for Ba^{2+} sites in $Ba_5Al_3F_{19}$ lattice.

2.3.3. Synthesis process of $LiLa_2NbO_6:Mn^{4+}$ phosphors

A series of $LiLa_2Nb_{1-x}Mn_xO_6$ ($0.005 \leq x \leq 0.01$) phosphors were prepared by the conventional high-temperature solid-state reaction. The raw materials in the synthesis process are Li_2CO_3, La_2O_3, Nb_2O_5 and MnO_2 in analytical reagent. Based on the formula of $LiLa_2Nb_{1-x}Mn_xO_6$ ($0.005 \leq x$

≤0.01), required amounts of the raw materials were calculated and weighted exactly by an electronic balance, and then thoroughly ground for at least 30 min. To compensate the loss of lithium during the sintering process, 20 % excess amount of Li_2CO_3 was added. The $LiLa_2Nb_{1-x}Mn_xO_6$ ($0.005 \leq x \leq 0.01$) compound was synthesized according to the following chemical reaction:

$$Li_2CO_3(+20mol\%)+2La_2O_3+2xMnO_2+(1-x)Nb_2O_5 \rightarrow 2LiLa_2Nb_{1-x}Mn_xO_6$$

After fully grinding, the samples were placed in a covered alumina crucible and then heated at 900 ^oC in air for at least 24 hours due to the slow decomposition rate of Li_2CO_3 in the molten state. Afterwards, the samples were ground again in order to improve the homogeneity and heated for 8 hours at 1100 ^oC in air.

2.4. Characterization

In this work, the obtained products are characterized by X-ray diffraction (XRD) using a Philips X'Pert MPD (Philips, Netherlands) X-ray diffractometer at 40 kV and 30 mA. All patterns are recorded in the range of 10-90°with a step size of $\Delta 2\theta$= 0.02.The morphology, particle size and energy dispersive spectrometer (EDS) of the phosphor are characterized by scanning electron microscope (SEM) system (JSM-6490, JEOL Company). The ultraviolet-visible diffuse reflectance spectrum is recorded using a V-670 (JASCO) UV-vis spectrophotometer. The photoluminescence excitation (PLE) spectra are recorded by a Pjoton

Technology International (PTI, USA) fluorimeter with a 60 W Xe-arc lamp as the excitation light source at room temperature. The photoluminescence (PL) spectra and decay lifetimes are collected by a 266 nm-pulsed Nd: YAG laser with a pulse width of 5 ns and a repetition rate of 10 Hz (Spectron Laser Sys. SL802G). The luminescence was dispersed by the 75cm monochromator (ActonResearch Corp. Pro-750, Acton, MA) and multiplied by the PMT (Hamamatsu R928, Hamamatsu Electronic Press Co., Ltd., Shizuoka, Japan).

3. Synthesis, structure and optical performance of red-emitting phosphor $Ba_5AlF_{13}:Mn^{4+}$

3.1. Introduction

Compared with traditional oxide lattices, fluoride lattices have rich advantages; for examples, the lower phonon energy, high refractive index, high quantum efficiency, and high thermal stability.[49] From the viewpoint of low quenching possibility of the excited states of the dopant ions, many fluoride lattices have been chosen as phosphors with some activators. Mn^{4+}, as a transition metal ion with an unfilled $3d^3$ electron shell, plays an important role in lighting and display fields.[50] Contrary to the rare-earth-ions with the parity-forbidden *f-f* transition, the luminescence properties of Mn^{4+} with the d-d transition are easily influenced by various coordinated environmental factors. In fluoride lattices, Mn^{4+} prefers to occupy the site with octahedral coordination on which the strong crystal field acts. Therefore, the Mn^{4+} ions exhibit the intense broad absorption band in the wavelength region near UV - 550 nm and a series of sharp emission lines peaking at around 630 nm.[51] Due to these characteristics, considerable attention has been focused on this field.

A series of Mn^{4+} activated red phosphors with high luminous efficacy have been reported as candidates of red-emitting phosphors, especially,

Mn^{4+}-doped fluoride hosts. Mn^{4+}-activated microcrystals K_2TiF_6 were successfully synthesized by Zhu et al in 2014.[33] The K_2TiF_6 microcrystals present strong line emission with high luminescence quantum yield as high as 98%, high thermal stability, and extremely high emission intensity. Mn^{4+}-doped alkaline hexa-fluorides, $B_2XF_6:Mn^{4+}$ (B = K, Cs, Rb; X = Ti, Si and Ge) have been well known as excellent red-emitting phosphors for warm w-LEDs.[52][53] However, it deserves to further explore novel Mn^{4+}-doped fluorides for red phosphors and more deep investigations should be carried out.

Here, in this work, we choose Mn^{4+}-doped fluoride Ba_5AlF_{13} as a red-emitting phosphor, which has not yet been reported in literatures to our best knowledge. The $Ba_5AlF_{13}:Mn^{4+}$ nanoparticles were synthesized via the two-step coprecipitation method. The phase formation, morphology features, excitation and emission spectra and thermal quenching behaviours are further investigated. The obtained product possesses a red line-emission spectrum with high thermal stability, which has the potential to enhance the color rendering index of an LED device.

3.2. Results and discussion

3.2.1. Structural characterization

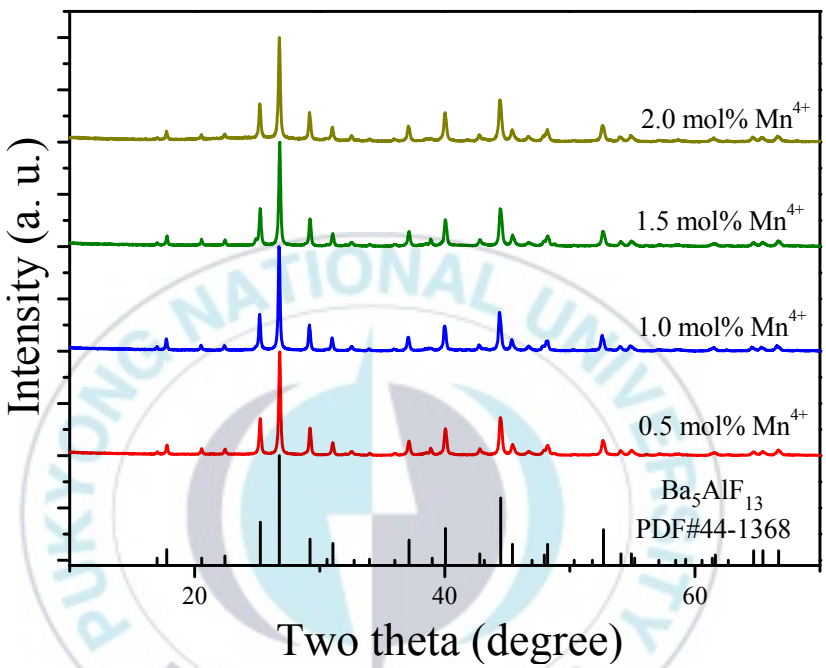

Fig. 3-1 X-ray diffraction patterns of $Ba_5AlF_{13}:Mn^{4+}$ nanoparticles as functions of Mn^{4+} concentration. The PDF card is displayed for comparison.

Fig. 3-1 shows the XRD patterns of the $Ba_5AlF_{13}:Mn^{4+}$ nanoparticles as functions of Mn^{4+} concentration. The standard PDF card (PDF#44-1368) is displayed for comparison. All the diffraction peaks match well with the standard PDF card, indicating that the $Ba_5AlF_{13}:Mn^{4+}$ nanoparticles with different Mn^{4+} concentration have been prepared as desired through the

two-step coprecipitation method. The $Ba_5AlF_{13}:Mn^{4+}$ nanoparticles crystallize in a cubic space group Fd-$\bar{3}$m. The unit cell parameters are a=b=c=17.378 Å, α=β=γ=90°, V=4427.83 $Å^3$ and Z=3.[54] Although Ba_5AlF_{13} and K_2MnF_6 have different crystal structures and there is a mismatch in the valence states between Al^{3+} and Mn^{4+}, the Mn^{4+} ions can also be incorporated into the host lattice of Ba_5AlF_{13} due to the similar ionic radii of Mn^{4+} (CN=6, 0.53 Å) in [MnF_6] and Al^{3+} (CN=6, 0.535 Å) in [AlF_6].[55]

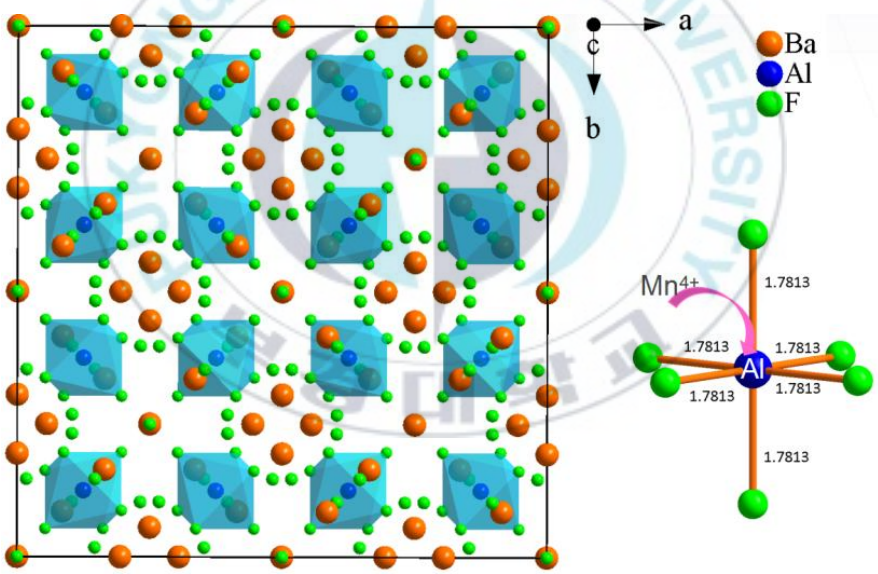

Fig. 3-2 Unit cell of the cubic-type Fm-$\bar{3}$m crystal structure of Ba_5AlF_{13} projected along c axis and coordination of the Al^{3+}/Mn^{4+} ion in such a cubic-type crystal structure. Ba, F, and Al/Mn ions are represented with orange, green, and blue spheres, respectively.

Fig. 3-2 shows the structural map of Ba_5AlF_{13} and $[AlF_6]$ octahedron according to the atomic coordinate's data from reference. The Ba_5AlF_{13} lattice consists of only one kind of crystallographic site of Al^{3+}. All the Al^{3+} ions are located at the center of the regular octahedron $[AlF_6]$, while Ba^{2+} forms $[Ba_{(2)}F_8]$ and $[Ba_{(1)}F_{10}]$ polyhedra connected together with $[AlF_6]$ octahedra. Since the ionic radius (0.530 Å) of Mn^{4+} is a little smaller than that (0.535 Å) of Al^{3+}, the Mn^{4+}-F^- distance is probably smaller than Al^{3+}-F^- distance. This means that a distorted system $[MnF_6]$ octahedron is preserved.

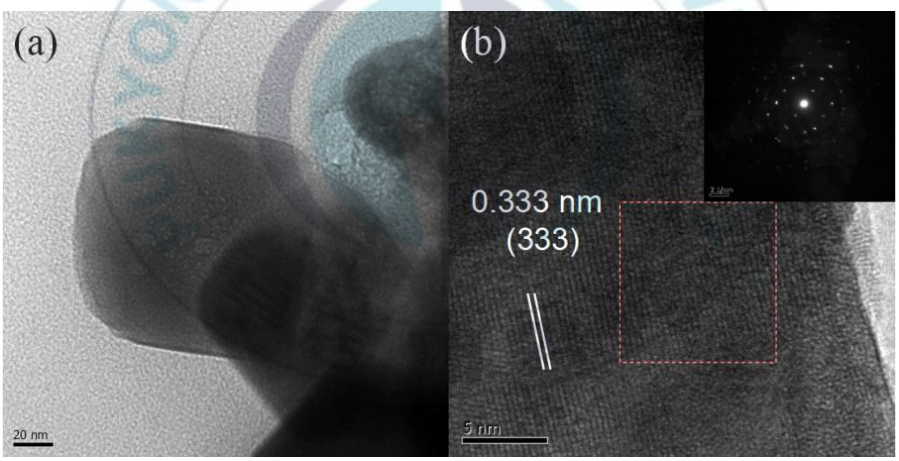

Fig. 3-3 Typical TEM image (a), HRTEM image (b), and the selected area electron diffraction pattern (the inset of b) of Ba_5AlF_{13}:Mn^{4+} nanoparticles.

The actual size and morphology of the particles were analysed by TEM. **Fig. 3-3a** is the typical TEM image of Ba_5AlF_{13}:Mn^{4+} nanoparticles. The size of the nanoparticles is estimated to be about 120 x 120 nm^2. **Fig.**

3-3b shows the high-resolution TEM image (HRTEM) confirming the single-crystalline nature of the $Ba_5AlF_{13}:Mn^{4+}$ nanoparticles. In addition, the selected area electron diffraction (SAED) pattern (the inset of **Fig. 3-3b**) exhibits the cubic symmetry ascribed to $Ba_5AlF_{13}:Mn^{4+}$ nanoparticles. The spacing of 3.33 Å corresponds to the (333) reflection of the $Ba_5AlF_{13}:Mn^{4+}$ nanoparticles.

3.2.2. Spectroscopic properties of Mn^{4+} ions in Ba_5AlF_{13}

The level scheme of Mn^{4+} in the lattice can be described by using the Tanabe-Sugano diagram and configuration coordinate model as shown in **Figs. 3-4a** and **b**, respectively. The luminescence characteristics of the Mn^{4+} ions depend highly on the crystal field strength except for the $^2T_{1g}$ and ^2E_g states. The excitation spectrum of Mn^{4+} corresponds to the spin allowed $^4A_{2g}\rightarrow{}^4T_{2g}$ and $^4A_{2g}\rightarrow{}^4T_{1g}$ transitions, while the emission spectrum belongs to the spin-forbidden *d-d* transition from the ^2E_g state to the $^4A_{2g}$ state as in **Fig. 3-4b**. The lateral displacement between the parabolas of ground state $^4A_{2g}$ and excited state $^4T_{1g}$ (or $^4T_{2g}$) is large, while a small displacement between the parabolas of $^4A_{2g}$ and ^2E_g. The larger displacement implies the stronger electron-phonon interaction giving rise to the larger spectral bandwidth of the transition.[56] Thus intense excitation bands with relatively large bandwidths are expected for the transitions between these states, meanwhile, sharp emission lines due to the $^2E_g\rightarrow{}^4A_{2g}$ transition of Mn^{4+}.

The room temperature excitation spectrum of $Ba_5AlF_{13}:Mn^{4+}$ (0.5 mol%) are shown in **Fig. 3-4c**. The excitation spectrum is composed of two

broad bands with the maxima at 360 and 460 nm corresponding to the spin allowed $^4A_{2g}\rightarrow{}^4T_{1g}$ and $^4A_{2g}\rightarrow{}^4T_{2g}$ transitions of Mn^{4+}, respectively. The slightly splitting phenomenon can be observed in the excitation band corresponding to the $^4A_{2g}\rightarrow{}^4T_{2g}$ transition but not observed for the $^4A_{2g}\rightarrow{}^4T_{1g}$ transition, probably due to a strong overlap with the re-absorption band of $^4A_{2g}\rightarrow{}^4T_{1g}$ and $^4A_{2g}\rightarrow{}^2E_g$ transitions.[57] The excitation spectrum indicates that the red phosphor doped with Mn^{4+} can be effectively excited by near UV-blue light, which is especially ideal for blue light excitation LED chips.

Contrary to the excitation spectrum, the emission spectrum belongs to the spin-forbidden *d-d* transition from the ^2E_g state to the $^4A_{2g}$ state of Mn^{4+}, as shown in **Fig. 3-4d**. The emission spectrum consists of several sharp lines with the main peak at 627 nm. In general, the zero-phonon line (ZPL) of Mn^{4+} in fluoride lattices is located at around 620 nm.[58] The three peaks longer than 620 nm belong to Stokes v_6 (t_{2u} bending), v_4 (t_{1u} bending), and v_3 (t_{1u} stretching) modes, whereas the two peaks shorter than 620 nm belong to anti-Stoke v_6 (t_{2u} bending) and v_4 (t_{1u} bending) modes. The ZPL is not observable for the high symmetrical environment of the lattice, for examples, $Rb_2SiF_6:Mn^{4+}$ and $BaTiF_6:Mn^{4+}$ red phosphors.[59] The more distorted coordination environments cause the stronger intensity of the ZPL line.[60] The intense ZPL observed in the emission spectrum of the $Ba_5AlF_{13}:Mn^{4+}$ nanoparticles indicate that the Mn^{4+} ions experience a lower crystal field symmetry which is mainly due to the distorted $[MnF_6]$ octahedron in the $Ba_5AlF_{13}:Mn^{4+}$ lattice. According to reference, the

existence of ZPL emission in a Mn^{4+} doped phosphor can further improve the color rendering index. The CIE chromaticity coordinates of $Ba_5AlF_{13}:Mn^{4+}$ are calculated to be (x=0.691, y=0.31), which are close to the national television system committee (NTSC) standard values for red color (x=0.67, y=0.33).

The local crystal field strength Dq and two Racah parameters B and C can be introduced to describe the unique energy levels of the Mn^{4+} ions in Ba_5AlF_{13} lattice.[61] The local crystal field strength Dq is given by the mean peak energy of the $^4A_{2g} \rightarrow {}^4T_{2g}$ transition and written by the following equation:

$$D_q = E(^4A_{2g} - {}^4T_{2g})/10 \qquad (3\text{-}1)$$

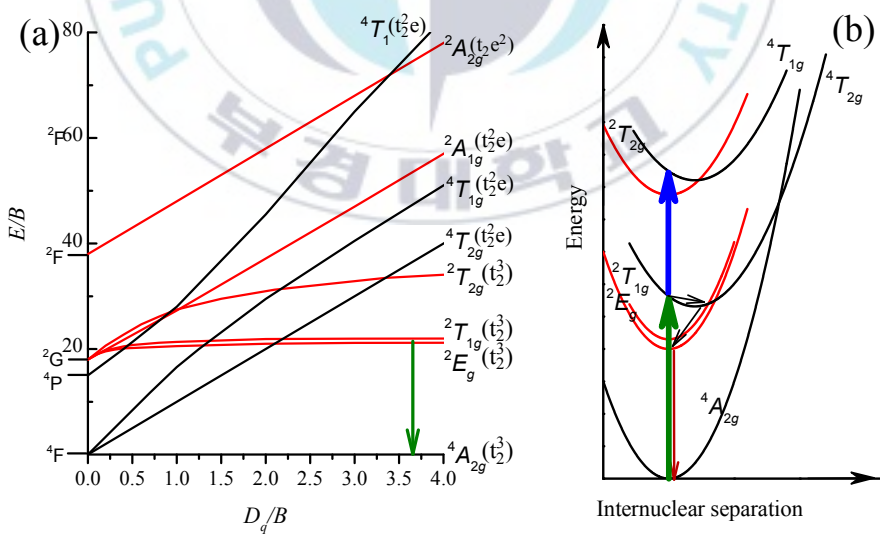

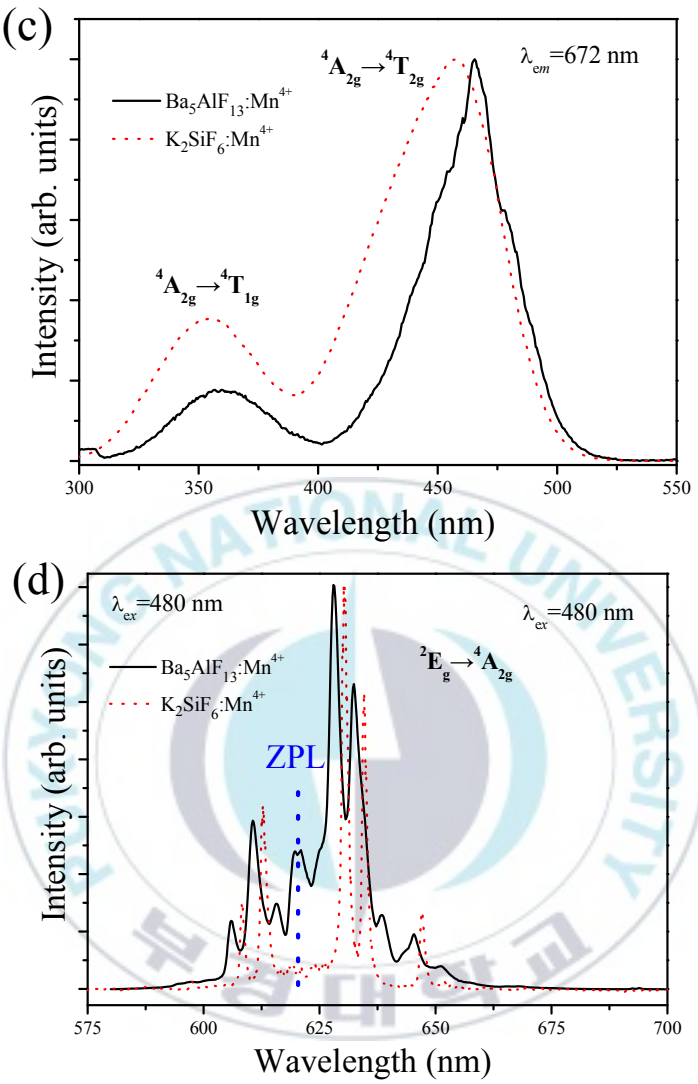

Fig. 3-4 (a) Tanabe-Sugano energy-level diagrams for $3d^3$ ions in the octahedral coordinate environment. **(b)** Configurational coordinate diagram for Mn^{4+} ions in fluoride hosts. Normalized excitation spectrum **(c)** and emission spectrum **(d)** of $Ba_5AlF_{13}:Mn^{4+}$ (0.5 mol%) compared with the K_2SiF_6:1%Mn^{4+} red phosphor.

In this work, 10Dq is estimated to be 21500 cm^{-1} from the excitation spectrum. On the basis of the peak energy difference (11900 cm^{-1}) between the $^4A_{2g} \rightarrow {}^4T_{2g}$ and $^4A_{2g} \rightarrow {}^4T_{1g}$ transitions, the Racah parameters B and C can be evaluated by the expressions:

$$\frac{D_q}{B} = 15(x-8)/(x^2-10x) \qquad (3\text{-}2)$$

$$\frac{E(^2E_g - {}^4A_{2g})}{B} = \frac{3.05C}{B} + 7.9 - \frac{1.8B}{D_q} \qquad (3\text{-}3)$$

where the constant x is defined as

$$x = \frac{E(^4A_{2g} - {}^4T_{1g}) - E(^4A_{2g} - {}^4T_{2g})}{D_q} \qquad (3\text{-}4)$$

From **Eqs. (3-2)** to **(3-4)**, the crystal field parameters of B and C are calculated to be 587 and 3800 cm^{-1}, respectively, which are comparable to those of $K_2SiF_6:Mn^{4+}$ (10Dq = 23900 cm^{-1}, B=605 cm^{-1}, C=3806 cm^{-1}).[62]

The well-known K_2SiF_6:1%Mn^{4+} red phosphor was prepared for comparison with the $Ba_5AlF_{13}:Mn^{4+}$ phosphor. The excitation spectrum of $Ba_5AlF_{13}:Mn^{4+}$ shifts to lower energy about 2400 cm^{-1} than that of $K_2SiF_6:Mn^{4+}$ as shown in **Fig. 3-4c**. This means that the crystal field strength of Mn^{4+} is weaker in Ba_5AlF_{13} lattice. As reported in Ref. 3, the 10Dq value depends on the metal-ligand distance with a relationship as $10Dq = K/R^n$, where K represents a constant and the value n is 5 approximately. As calculated in this work and refer to the Reference [58], the Al-F bond distance in $[AlF_6]$ group is 1.781 Å in Ba_5AlF_{13}, while the Si-F

bond distance in [SiF_6] group is 1.682 Å. Hence, the crystal field strength of Mn^{4+} is weaker in Ba_5AlF_{13} lattice, which is in consistent with the calculated 10Dq values above. As a consequence, the excitation spectrum of Ba_5AlF_{13}:Mn^{4+} shifts to lower energy. In addition, the luminescence intensity of K_2SiF_6:1mol%Mn^{4+} red phosphor is about three times higher than the phosphor prepared in this work.

Fig. 3-5 shows the emission spectra and decay curves of Ba_5AlF_{13}:Mn^{4+} nanoparticles as functions of Mn^{4+} concentration. No difference in spectral features between different Mn^{4+} concentrations is observed in the emission spectra except for the relative intensities of the phonon lines. The emission intensity increases with increasing Mn^{4+} concentration from 0.1 mol% and then reaches the maximum intensity at 0.5 mol%. Further increase in Mn^{4+} concentration, the emission intensity turns to decrease gradually because of the concentration quenching.[63] However, the emission intensity ratios (R) of the integrated ZPL intensity to the integrated v_6 line intensity depends on the Mn^{4+} concentration as shown in the inset of **Fig. 3-5a**. As mentioned above, the intensity of the ZPL depends highly on the local symmetry of the Mn^{4+} surroundings. The substitution of larger Mn^{4+} ion for the smaller Al^{3+} ion gives rise to the lattice distortion. Therefore, the higher Mn^{4+} concentration causes more distortion of the [MnF_6] octahedron lowering crystal field symmetry with the larger value R.

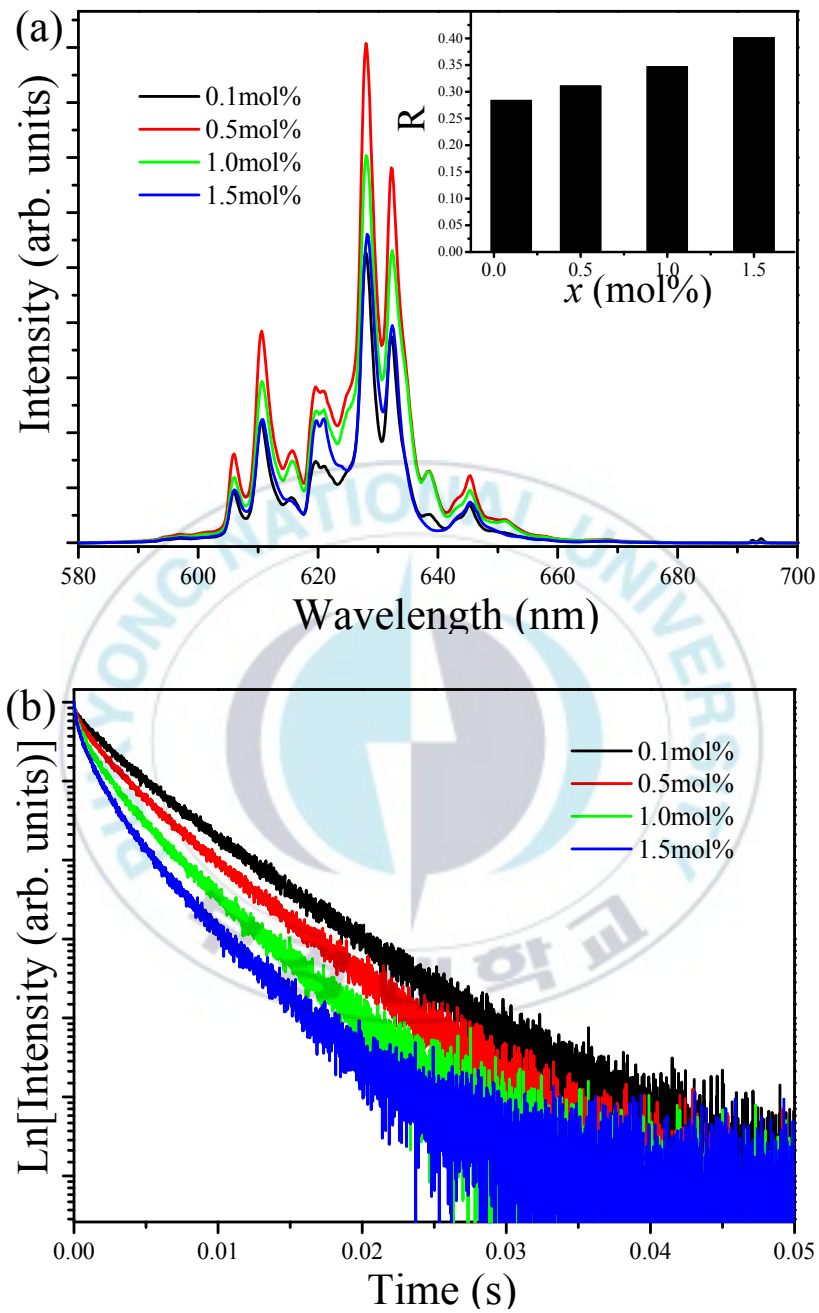

Fig. 3-5 Emission spectra (a) and decay curves (b) of $Ba_5AlF_{13}:Mn^{4+}$ nanoparticles as functions of Mn^{4+} concentration.

Fig. 3-5b shows the luminescence decay curves of $Ba_5AlF_{13}:Mn^{4+}$ (0.1 - 1.5 mol%) nanoparticles obtained by monitoring the 627 nm emission under the excitation of 355 nm. The average decay time τ can be calculated by using the equation.

$$\tau = \frac{\int_0^\infty tI(t)dt}{\int_0^\infty I(t)dt} \qquad (3\text{-}5)$$

The decay time decreases with increasing Mn^{4+} concentration and the decay curves gradually deviate from the single exponential. The decay times are estimated to be 8.03, 7.34, 6.07 and 5.13 ms for the Mn^{4+} concentration of 0.1, 0.5, 1.0 and 1.5 mol%, respectively. Since samples with low Mn^{4+} concentration would minimize the effects of interactions between the Mn^{4+} ions leading to nearly single exponential decay curves. However, with increasing Mn^{4+} concentration, the distance between the ions shortens; subsequently, the energy transfer between the Mn^{4+} ions can occur, which provides an additional decay channel, leading to a non-exponential decay curves. The possible explanation for this luminescence quenching is due to the higher nonradiative energy migration through a direct transfer among the Mn^{4+} ions.[64][65]

3.2.3. Unusual temperature-dependent emission spectra

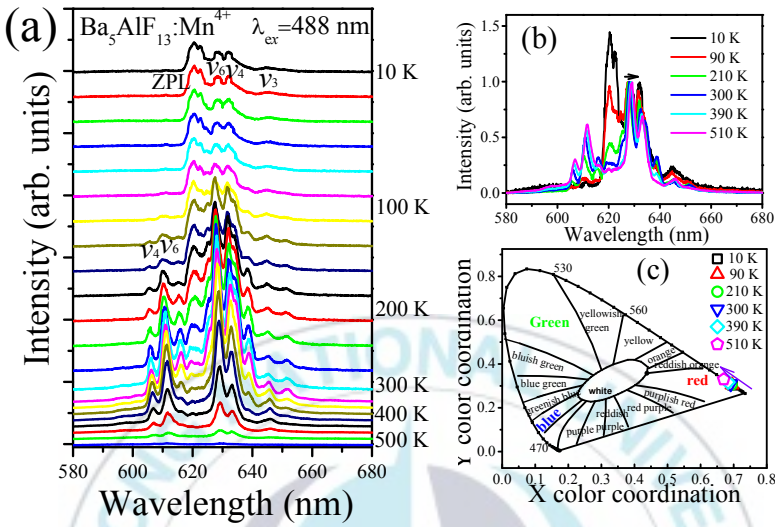

Fig. 3-6 Temperature dependent emission spectra (a) and normalized emission spectra (b) and CIE chromaticity coordinates (c) of $Ba_5AlF_{13}:Mn^{4+}$ (0.5 mol%).

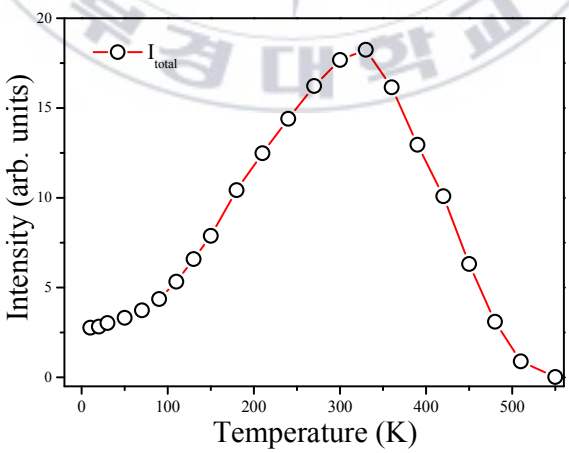

Fig. 3-7 Integrated intensity of total emission (Itotal) of $Ba_5AlF_{13}:Mn^{4+}$ as a function of temperature.

Fig. 3-6a shows the emission spectra of $Ba_5AlF_{13}:Mn^{4+}$ (0.5 mol%) as functions of temperature in the temperature region 10 - 500 K under excitation at 488 nm. As mentioned above, the emission lines are assigned to the spin-forbidden $^2E_g \rightarrow {}^4A_{2g}$ transition of Mn^{4+}, but can gain intensity by the activation of vibronic modes.[66] Some features are worth noting:

(1) The emission spectra show different spectral features in different temperatures. At 10 K, the peaks dominate on the low-energy side of the ZPL at 620 nm, while at T > 100 K the emission lines become broader and appear not only on the low-energy side but also on the high-energy side, which are known as the Stokes and anti-Stokes emission lines, respectively. At low temperature, the systems are more likely to be distributed in the vibrational ground state and Stokes emission primarily occurs. However, when temperature rises, electrons have enough energy to populate the upper vibration state and relax back to the ground state of $^4A_{2g}$ with anti-Stokes emission.[67]

(2) Based on the temperature dependent emission spectra in **Fig. 3-6a**, the total emission intensity as a function of temperature are shown in **Fig. 3-7**. The emission intensity increases firstly and then decreases with further increase in temperature. The emission intensity of a certain luminescent phosphor consistently decreases with the increase of temperature which is mainly due to the increase of the nonradiative transition probability.[68] However, differently from the most oxide lattices, Mn^{4+}-doped fluoride lattices exhibit anti-thermal quenching behavior.[69][70] As shown in **Fig. 3-7**, the total integrated emission

intensities of the $^2E_g \rightarrow {}^4A_{2g}$ transition at 300 K is found to be increased about 700% compared with the initial intensity at 10 K and then decreased due to the intense nonradiative transition. It is suggested for $Ba_5AlF_{13}:Mn^{4+}$ that the increased emission intensity is due to expansion of the host lattice and the enhancement of the lattice vibrations modes with increasing the temperature.[71]

(3) It is observed that all the emission peaks show a tiny red shift and become gradually broader with increasing temperature (**Fig. 3-6b**). This is mainly due to the expansion of the unit cell and the enhancement of the vibration modes of the $[MnF_6]^{2-}$ octahedral in a hot environment.[72]

(4) The shifts of emission peaks and the changes in the relative emission intensity may induce the variations of the chromatic coordinates of the phosphor. The dependences of the chromatic coordinates upon the temperature are calculated in Table 1 and shown in **Fig. 3-6c**. The x values slightly decrease, while the y values slightly increase with increasing temperature. The variation in chromatic coordinates is caused by the red-shift of emission bands and the enhancement of anti-Stokes bands.

Fig. 3-8 shows the decay curves of the 627 nm emission under the excitation of 355 nm as functions of temperature. The decays are single exponential at low temperature and become slightly non-exponential at high temperature. The decay times of the ^2E_g state are calculated by using

Eq. 3-5. The decay times decrease monotonically from 15.2 ms at 10 K to 1.28 ms at 520 K. The decay times calculated from the temperature-dependent decay curves are shown in **Fig. 3-9a**.

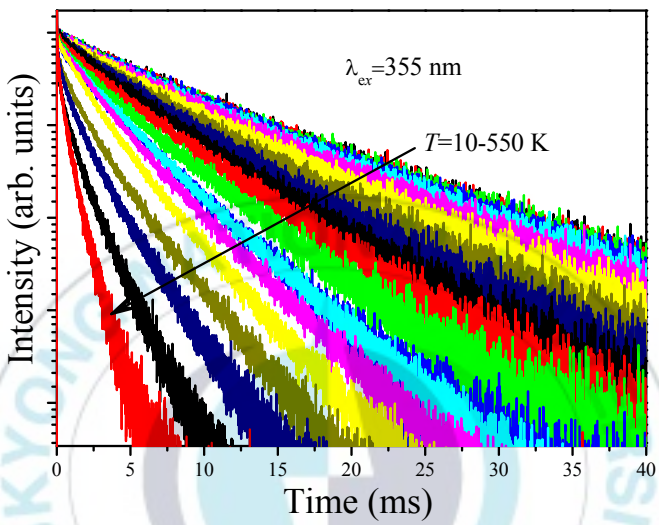

Fig. 3-8 Temperature dependent decay curves of $Ba_5AlF_{13}:Mn^{4+}$ obtained by monitoring the 627 nm emission under excitation at 355 nm.

The temperature dependent decay times of Mn^{4+} can be analyzed by the model for Cr^{3+} suggested by Grinberg.[73] Cr^{3+} is isoelectronic with Mn^{4+} ($3d^3$ configuration). According to this model, an additional relaxation pathway (the spin-allowed $^4T_{2g} \rightarrow {}^4A_{2g}$ transition) occurs with increasing temperature and the temperature dependent decay times can be written by the following equation.[74]

$$\tau = \frac{\tau_{stat}\left(1+\exp\left(-\frac{\hbar\omega_{-}}{kT}\right)+3\exp\left(-\frac{\Delta}{kT}\right)\right)}{\left(1+\frac{\tau_{stat}}{\tau_{dyn}}\exp(-\frac{\hbar\omega_{-}}{kT})\right)\left(\left(\frac{W_{so}}{\Delta'}\right)^{2}+3\exp\left(-\frac{\Delta}{kT}\right)\right)} \quad (3\text{-}6)$$

where the Δ' represents the energy difference between the ^2E_g and $^4T_{2g}$ states which can be calculated from the excitation spectrum. Δ is the energy difference between the minimum energy of the ^2E_g and $^4T_{2g}$ states. ħω- is considered as a free parameter for the effective energy of phonons and W_{SO} is an average spin-orbit parameter. $\frac{\tau_{stat}}{\tau_{dyn}}$ is the ratio of the radiative decay times induced by static and dynamic process. In addition, $\frac{1}{\tau_{dyn}}$ is explicitly independent on temperature.

The temperature dependent decay times are well fitted to **Eq. (3-6)** and the fit result is shown by the solid red curve in **Fig. 3-9a**. The best fit result gives the parameters Δ'=5150 cm^{-1}, Δ= 3170 cm^{-1}. ħω= 339 cm^{-1}, W_{SO}= 24 cm^{-1}, τ_{stat}= 0.311 μs and $\frac{\tau_{dyn}}{\tau_{stat}}$=7.3. The results of the temperature dependent decay times of the ^2E_g state means that an additional relaxation pathway (the spin-allowed $^4T_{2g}\rightarrow{}^4A_{2g}$ transition) due to the spin-orbit interaction of ^2E_g and $^4T_{2g}$ states occurs with increasing temperature. As calculated, the obtained values of radiative lifetime τ_{stat} related to $^4T_{2g}\rightarrow{}^4A_{2g}$ is 0.311 μs, which is much shorter than observed $^2E_g\rightarrow{}^4A_{2g}$ transition. And the effective spin-orbit coupling energy (24 cm^{-1}) is much smaller than the spin-orbit coupling energy of the spin-orbit interaction Hamiltonian by vibronic overlap integrals between the involved states as products of the electronic and vibronic wave functions.

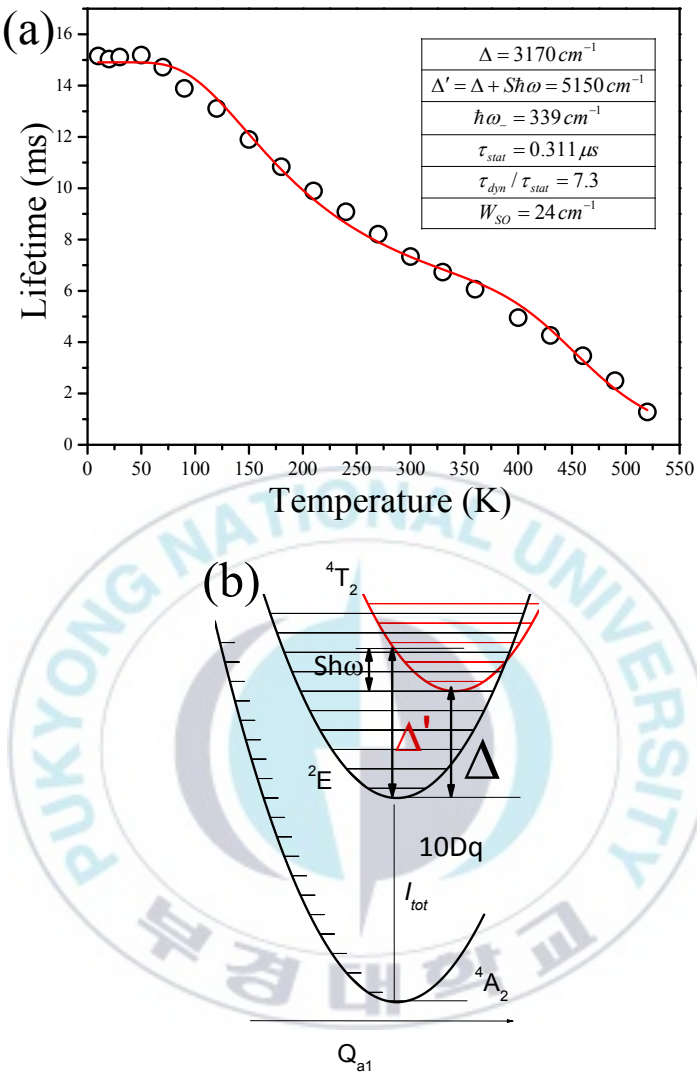

Fig. 3-9 (a) Decay times of the ^{2}E state as a function of temperature (10-550 K) for $Ba_5AlF_{13}:Mn^{4+}$ (0.5 mol%). (b) The diagram that includes the ground state and the lowest excited states without spin-orbit interaction.

4. Optical performance of the $Ba_5Al_3F_{19}:Eu^{2+}$ blue phosphors with high thermal stability

4.1. Introduction

Eu^{2+} ($4f^7$) ions as an excellent activator for phosphors have been extensively studied for many years due to the strong absorption and luminescence intensity, and the emission wavelength covers from red to ultraviolet.[75][76] The typical strong absorption and emission of Eu^{2+}-doped phosphors originate from the optical transition between the excited $4f^65d$ state and the ground $4f^7$ ($^8S_{7/2}$) state (hereafter *d-f* transition). And the transition from the lowest excited $4f^7(^6P_{7/2})$ state to the ground $f^7(^8S_{7/2})$ state (hereafter *f-f* transition) usually cannot be observed due to the $4f^65d$ state located at lower energy than the $4f^7(^6P_{7/2})$ state. However, when the nephelauxetic effect and the crystal field strength acting on Eu^{2+} ions are too weak to push up the $4f^65d$ state over the $4f^7(^6P_{7/2})$ state, the forbidden *f-f* transition can be observed.[77] The examples are $KMgF_3:Eu^{2+}$,[78] $BaY_2F_8:Eu^{2+}$,[79] $Mg_3(BO_3)F_3:Eu^{2+}$,[80] etc.

Here, the luminescence properties of Eu^{2+} in $Ba_5Al_3F_{19}$, which have not yet been reported as a blue phosphor in the literature to our best knowledge, were investigated on the following motivations. Firstly, metal fluorides compared with the oxygen-based matrix have some comparative advantages as matrices for lower phonon energy, high refractive index, high quantum efficiency, and high chemical and mechanical properties.

This could significantly improve the thermal stability from the viewpoint of reducing the thermal quenching of the excited states of the activator ions.[81] In addition, an efficient broad band emission around 410 nm can be observed due to the *d-f* transition of Eu^{2+} ions along with the sharp *f-f* transition around 360 nm, which were firstly reported in $Ba_5Al_3F_{19}$ matrix.

In current work, Eu^{2+} doped $Ba_5Al_3F_{19}$ phosphors were prepared by simple solid state method. The crystallographic sites and the doping mechanism of Eu^{2+} ions in $Ba_5Al_3F_{19}$ are investigated in detail. Furthermore, the temperature-dependent luminescence spectra and decay curves were used to investigate the doping mechanism of Eu^{2+} ions and confirm the thermal stability of Eu^{2+} doped $Ba_5Al_3F_{19}$ phosphors.

4.2. Results and discussion

4.2.1. Phase identification

Fig. 4-1 shows the XRD patterns of the as-prepared $Ba_{5(1-x)}Al_3F_{19}:5xEu^{2+}$ (x=0.001 - 0.04) phosphors together with the standard PDF card of $Ba_5Al_3F_{19}$ (PDF2 No.48-0193). All the reflection peaks are observed to be in agreement well with the standard $Ba_5Al_3F_{19}$ phase with a tetragonal space group of I 4/m. No extra diffraction peaks belong to impurities can be detected, indicating that the dopants Eu^{2+} completely enter the lattice of the as-prepared phosphors.

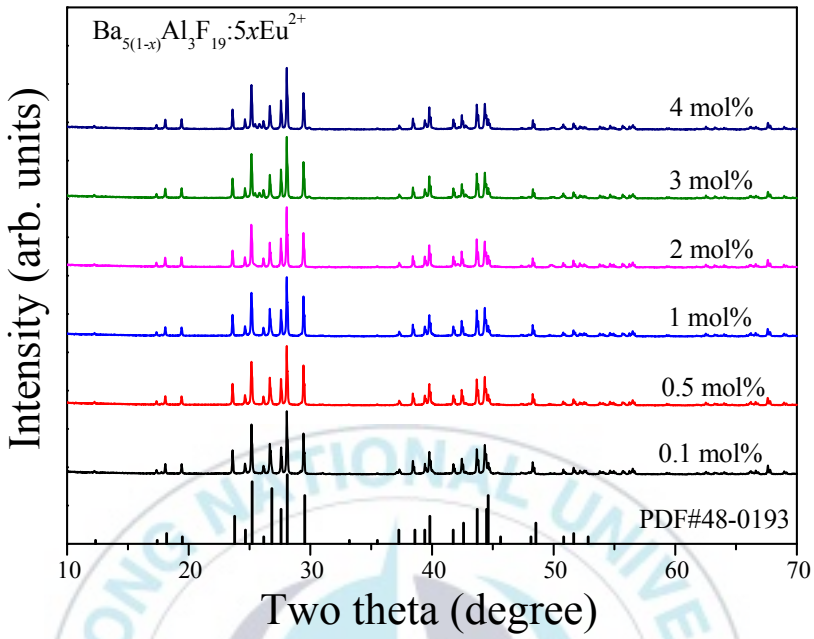

Fig. 4-1 The XRD patterns of $Ba_{5(1-x)}Al_3F_{19}:5xEu^{2+}$ (x=0.001, 0.005, 0.01, 0.02, 0.03, 0.04) compared with the standard pattern card PDF2 No.48-0193.

4.2.2. Luminous origin of $Ba_5Al_3F_{19}:Eu^{2+}$ phosphors

Fig. 4-2 shows the typical excitation and emission spectra of $Ba_5Al_3F_{19}:0.02Eu^{2+}$ phosphor. The excitation spectrum monitored at 410 nm consists of a broad band in the wavelength region 200 - 400 nm. The excitation band is assigned to the *d-f* transition of Eu^{2+}. Obviously, the excitation spectrum covers UV to blue region indicating that $Ba_5Al_3F_{19}:Eu^{2+}$ phosphors can be used as UV - blue excited blue-emitting phosphor. The emission spectrum under the excitation of 310 nm consist

of a asymmetric band peaked at 410 nm ascribed to the *d-f* transition.

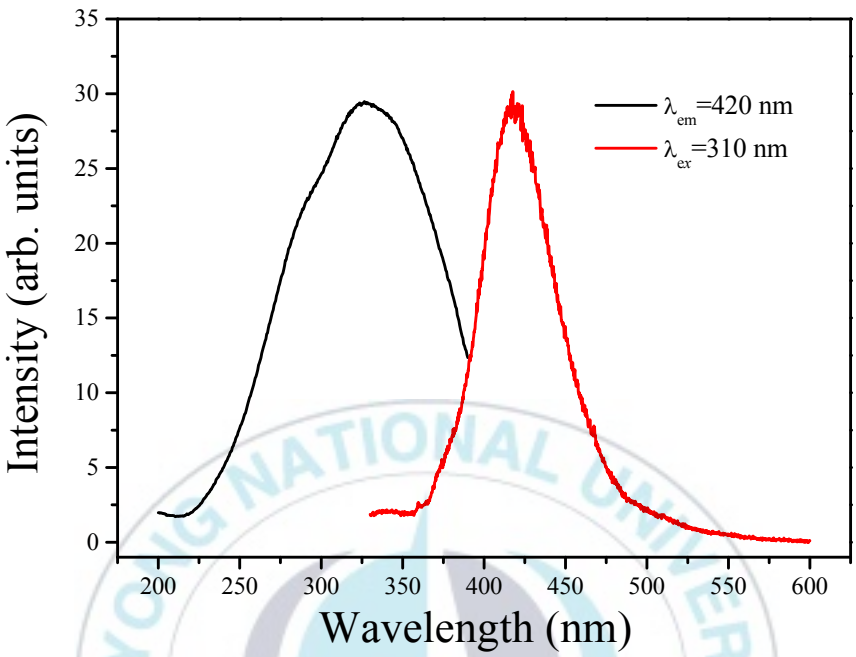

Fig. 4-2 Low resolution excitation and emission spectra of $Ba_5Al_3F_{19}$:0.02Eu^{2+} at room temperature.

Fig. 4-3a shows the highly resolved room temperature emission spectra of $Ba_{5(1-x)}Al_3F_{19}$:5$x$$Eu^{2+}$ (x = 0.01 -0.4) obtained under the excitation of 266 nm. All the emission spectra consist of a sharp line at 360 nm corresponding to the *f-f* transition of Eu^{2+} together with the broad band with a maximum around 410 nm ascribed to the *d-f* transition of Eu^{2+}. The line emission is discussed in the next Section. As shown in **Fig. 4-3b**, the luminescence intensity increases with increasing Eu^{2+} concentration and reaches a maximum intensity at 1 mol%. However, when the doping concentration is higher than 1 mol%, the luminescence intensity saturates

and then decreases due to the concentration quenching, mainly resulting from the nonradiative energy transition among the identical activator Eu^{2+} ions.[82] Generally, nonradiative transition was attributed to radiation reabsorption, exchange interaction or electric multipolar interaction.[83] The critical distance (R_c) between the nearby Eu^{2+} ions can be estimated by the following equation:[84]

$$R_c \approx 2\left(\frac{3V}{4\pi x_c N}\right)^{1/3} \qquad \textbf{(4-1)}$$

Where x_c is the critical concentration, V represents the volume of unit cell and N refer to the number of formula units per unit cell. Here, N=4, x_c=0.01, and V=1584.84 $Å^3$. Thus, R_c is calculated to be 21.15 Å. As reported, the exchange interaction commonly occurs in the forbidden transition, that is to say, the nonradiative transition among the Eu^{2+} ions in $Ba_5Al_3F_{19}$ phosphors should be controlled by electric multipolar-multipolar interaction. According to the report of Van Uitert, the interaction type between sensitizers can be calculated by the following equation:[85]

$$\frac{I}{x} = \frac{k}{1+\beta(x)^{\theta/3}} \qquad \textbf{(4-2)}$$

where I represents the emission intensity, x represents the activator concentration, k and β are constants for a given matrix under the same measurement conditions. The types of nonradiative energy transfer can be indicated by the value of θ. θ = 6, 8, and 10, stand for electric

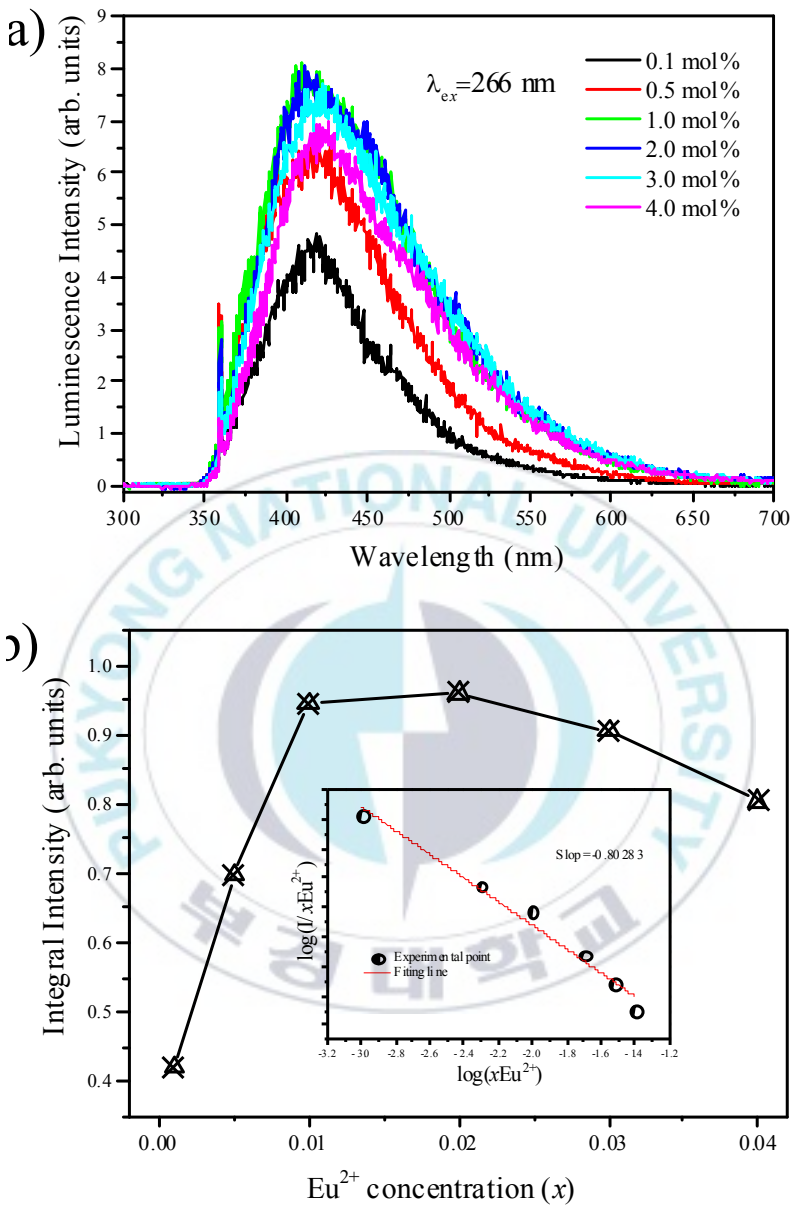

Fig. 4-3 (a) Highly resolved room temperature emission spectra of $Ba_{5(1-x)}Al_3F_{19}:5xEu^{2+}$ as functions of Eu^{2+} concentration. (b) Dependence of the integrating intensity on the doping concentration of Eu^{2+}. The inset in (b) shows the dependence of $lg(I/xEu^{2+})$ on $lg(xEu^{2+})$ for $Ba_{5(1-x)}Al_3F_{19}:5xEu^{2+}$.

dipole-dipole, dipole-quadrupole, and quadrupole-quadrupole interactions, respectively and θ = 3 stands for the energy transfer between nearest Eu^{2+} ions.[86]

The relationships of log(I/*x*) *vs* log*x* are shown in the inset of **Fig. 4-3b** and the slope of the fitting line is -0.80283. Hence, the value of θ is calculated to be to 2.41 and approximately equal to 3, which means that the dominant concentration quenching mechanisms between Eu^{2+} ions occur via energy transfer between nearest Eu^{2+} ions.

4.2.3. Luminescent decays for different Eu^{2+} concentration

In order to describe the concentration quenching behavior and confirm the origin of the line emission at 360 nm in more detail, a series of decay curves for $Ba_{5(1-x)}Al_3F_{19}:5xEu^{2+}$ phosphors are measured under the excitation of the 266 nm pulsed laser. Due to the weak nephelauxetic effect and the crystal field strength in fluoride phosphors (push up the $4f^6 5d$ state over the $4f^7(^6P_{7/2})$ state), the forbidden *f-f* transition around 360 nm can be observed. The decay time (**Fig. 4-4a**) of the forbidden *f-f* transition (360 nm) is much longer than that (**Fig. 4-4b**) of the allowed *d-f* transition (410 nm).[87]

As shown in **Figs. 4-4a** and **b**, both decays of 360 and 410 nm emissions are non-exponential. The non-exponential decay curves may be caused by some energy transfer and the possible multisite structure of Eu^{2+} ions.[88] Otherwise, the luminescence decay times of the *f-f* and *d-f*

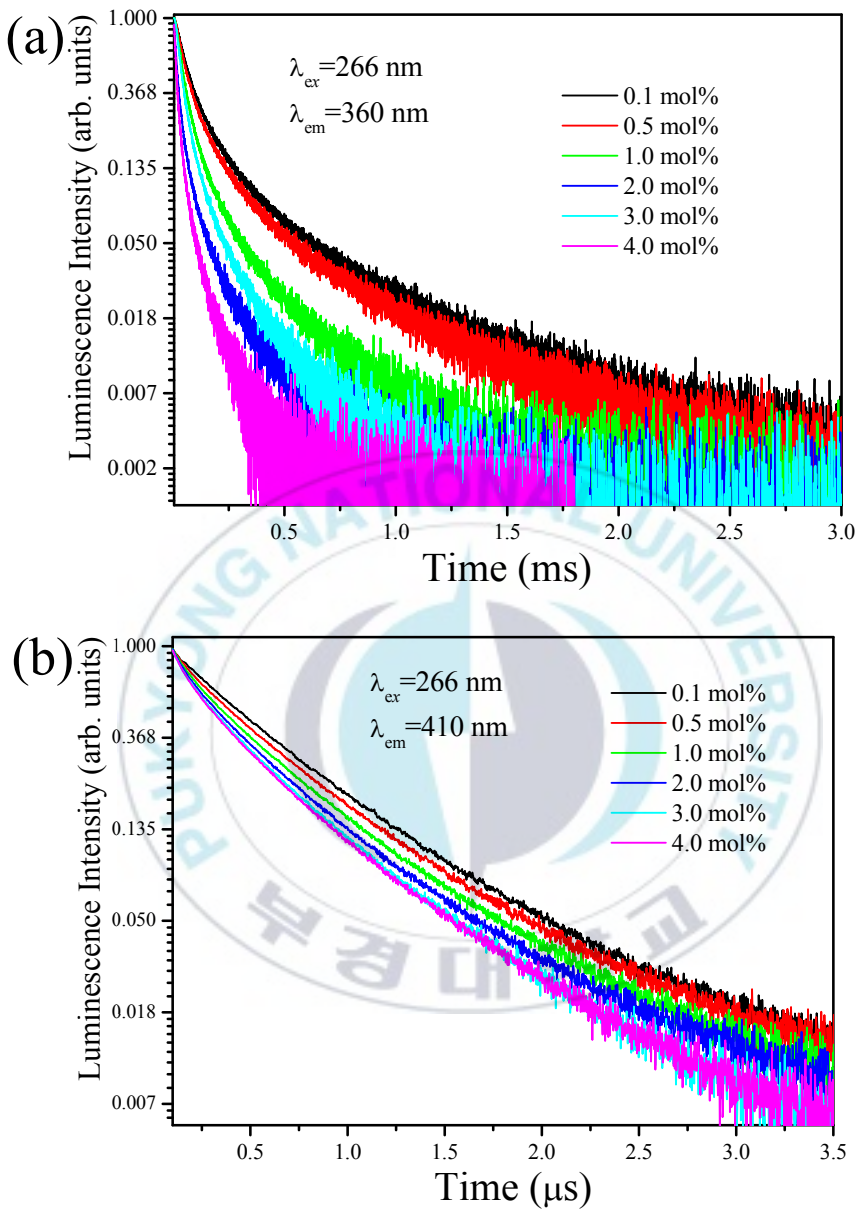

Fig. 4-4 Decay curves of the emissions at 360 nm (a) and 410 nm (b) of $Ba_{5(1-x)}Al_3F_{19}:5xEu^{2+}$ (x=0.001, 0.005, 0.01, 0.02, 0.03, 0.04) under the excitation of 266 nm.

transitions decreases with increasing Eu^{2+} concentration. The decrease of the decay times can be ascribed to the increases of the energy transfer rate between the Eu^{2+} ions and the probability of energy transfer to luminescent killer sites.[89][90] The decay times can be characterized by the average decay time (τ) by using the following equation:[91]

$$\tau = \frac{\int_0^\infty tI(t)dt}{\int_0^\infty I(t)dt} \qquad \textbf{(4-3)}$$

Based on the **Eq. (4-3)**, the average decay time values were calculated to be 0.678, 0.520, 0.302, 0.185, 0.152, 0.110 ms for *f-f* transition and 1.16, 1.15, 0.99, 0.85, 0.72, 0.66 μs for *d-f* transitions in the series of $Ba_{5(1-x)}Al_3F_{19}:5xEu^{2+}$ phosphors, respectively.

4.2.4. Temperature dependent emission for Eu^{2+}

Fig. 4-5 shows temperature-dependent emission spectra obtained in the temperature region from 10 to 300 K under the excitation of 310 nm. Two broad bands around 410 nm due to the *d-f* transitions of Eu^{2+} are observed together with the sharp lines around 360 nm in all temperature regions. It is worth noting that the emission line at 360 nm due to the *f-f* transition is nearly independent of the matrix because the 4*f* electrons are shielded by the $5s^25p^6$ electron clouds from the crystal field of the host. Usually, the transition from *f-f* is difficult to observe in most of the oxide hosts because the lower field component $4f^65fd$ ($^2t_{2g}$) locates below the $4f^7$($^6P_{7/2}$) level.

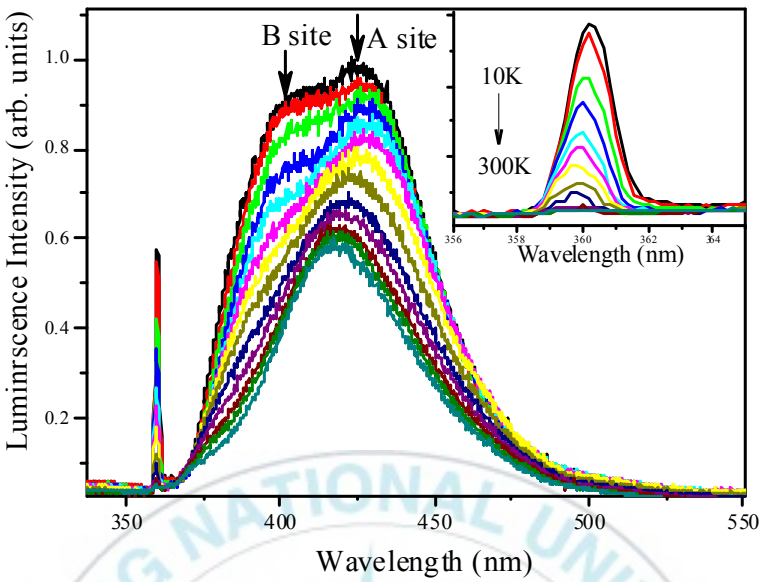

Fig. 4-5 Temperature-dependent emission spectra of $Ba_5Al_3F_{19}$:0.005Eu^{2+} excited by 310 nm, colored lines means the emission spectra at different temperature.

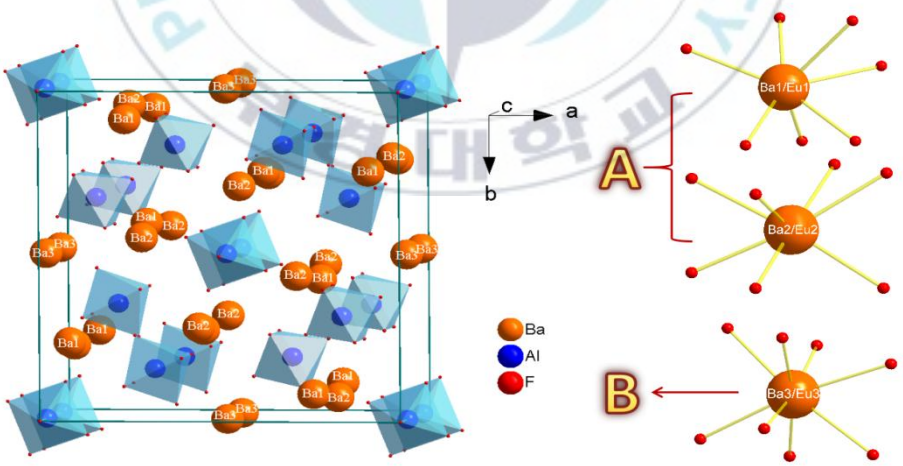

Fig. 4-6 The sketch map of $Ba_5Al_3F_{19}$ crystal structure modeled on the basis of the atomic coordinate's data obtained from the Reference.

For the weak field, for example, fluorides, the ^2e_g (tetrahedral symmetry) state may be higher than the $^6P_{7/2}$ state and thus the parity-forbidden *f-f* transition could be observed.[92] Such phenomenon has been reported, for examples, such as *f-f* transition peaked at 360 nm in $NaMgPO_4:Eu^{2+}$,[93] 360 nm in $LiMgPO_4:Eu^{2+}$,[94] 360 nm in $LiBaF_3:Eu^{2+}$,[95] 361 nm in $BaAlBO_3F_2:Eu^{2+}$[96] and so on. The sharp lines are always quenched with increasing temperature as shown in the insert of **Fig. 4-5**.

Otherwise, the spectral feature of broad band emission changes with the increase of temperature. The broad emission consists of two bands at 425 nm (band A) and 405 nm (band B) at 10 K and at the temperature higher than 100 K the two bands are indistinguishable. The appearance of two bands at low temperature is probably due to different emission centers with different coordination environments. The Eu^{2+} ions substitute for Ba^{2+} ions in the $Ba_5Al_3F_{19}$ lattice. According to the report of Martineau,[97] the $Ba_5Al_3F_{19}$ lattice contains two types of 6-fold coordinated Al atoms, three types of Ba atoms, and eight crystallographically inequivalent F atoms (**Fig. 4-6**). Ba_I and Ba_{II} are surrounded by seven nearest neighbor F^- ions in the form of decahedron which are more heavily distorted structure than that of the Ba_{III} site surrounded by eight F^- ions with regular hexahedron. The average distances between the central atoms and ligands of the three Ba atoms were calculated to be $R[Ba_I\text{-}F]$= 2.7026 Å, $R[Ba_{II}\text{-}F]$= 2.71344 Å, and $R[Ba_{III}\text{-}F]$= 2.71705 Å, respectively. Usually, the crystal field strength *D*q in inversely proportional to the 5th power of

the bond-length R: $Dq \propto 1/R^5$. So we concluded that the appearance of two bands at low temperature is due to the superposition of different emission centers with different crystal field strength Dq.[98] Besides, with increasing temperature, both of the two separated broad band emission decreases in intensity due to the thermal quenching behavior. The remarkable quenching of the emission intensity is around 405 nm ascribed to the B emission and a slight blue-shift of the A emission band is observed. Such a phenomenon can be described as the thermal activation from the higher excited states of B emission to the lower excited states of A emission, that is Energy transfer process. At temperatures higher than 100 K it seems that thermal equilibrium occurs between A and B emissions giving rise to the spectral feature with single band.

4.2.5. Thermal stability of the Eu^{2+} luminescence

Fig. 4-7 shows temperature dependent decay curves for the sharp line emission due to the *f-f* transition at 360 nm and the broad band emission due to the *d-f* transition at 410 nm. The decay time of the 360 nm emission is estimated to be 540 μs at 10 K, while that of the 410 nm band emission is 0.647 μs at 10 K.

The thermal stability is one of the important parameters for the obtained phosphors in potential application due to a considerable influence on the color rendering index (CRI) and light output.[99][100] Usually, the phosphors employed in LED devices are expected to operate above 150 ^{o}C. Thus the temperature dependent emission spectra and decay

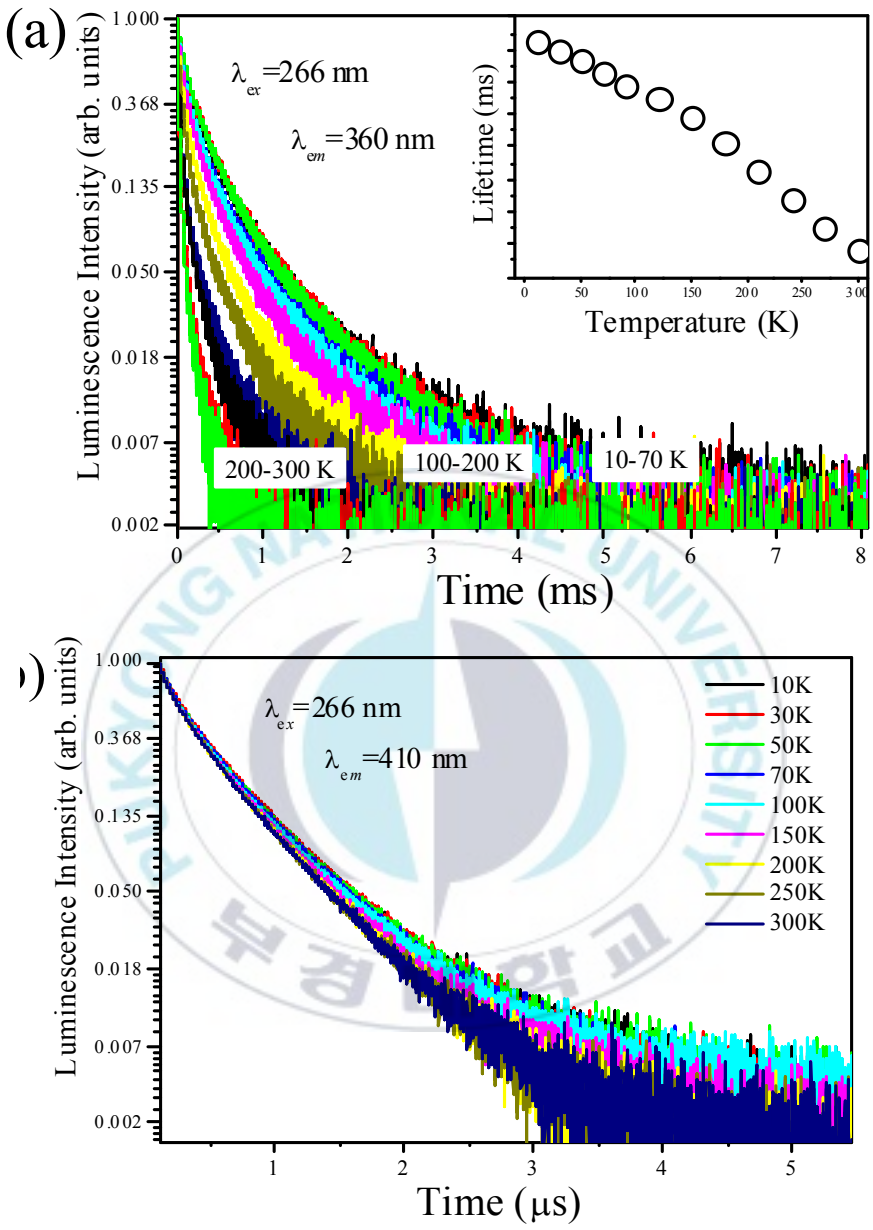

Fig. 4-7 Temperature-dependent decay curves of $Ba_5Al_3F_{19}$:0.005Eu^{2+} obtained by monitoring 360 (a) and 410 nm (b) emissions.

curves are measured and displayed in the temperature region 300 - 470 K as shown in **Fig. 4-8**. Obviously, with the increase of temperature, both of the emission intensities and the decay times decreased gradually. The luminescence intensity decreases to 70% (at 423 K) of the initial value (at 300 K).

To better understand the thermal quenching phenomenon for $Ba_5Al_3F_{19}:0.005Eu^{2+}$, the activation energy (ΔE) can be calculated using the Arrhenius equation based on the data insert in **Fig. 4-8**:[101][102]

$$I_T = \frac{I_0}{1+c\exp(-\frac{\Delta E}{kT})} \qquad \textbf{(4-4)}$$

$$\tau_T = \frac{\tau_0}{1+c\exp(-\frac{\Delta E}{kT})} \qquad \textbf{(4-5)}$$

where I_0 and τ_0 are the initial PL intensity and decay time of the phosphor at room temperature, respectively. I_T and τ_T are the PL intensities and decay times at different temperatures, the constant "c" is the frequency factor constant or also known as pre-exponential factor or Arrhenius factor. It indicates the rate of collision and the fraction of collisions with the proper orientation for the reaction to occur, k is the Boltzmann constant (8.62×10^{-5} eV) and ΔE is the activation energy for thermal quenching. According to the above two equations, the $\ln(I_0/I_T - 1)$ and $\ln(\tau_0/\tau_T - 1)$ against 1000/T are plotted in **Fig. 4-9** and the straight slope equals to ΔE. The activation energies are calculated to be 2637 and 2742 cm^{-1} for $Ba_5Al_3F_{19}:0.005Eu^{2+}$ calculated through temperature-dependent luminescence intensities and

decay times, respectively. Compared with other reported blue phosphors, for example, 1637 cm^{-1} for $Mg_2Al_4Si_5O_{18}:0.03Eu^{2+}$,[103] 1935 cm^{-1} for $KMg_4(PO_4)_3:0.01Eu^{2+}$,[104] 1452 cm^{-1} for $Ba_4Gd_3Na_3(PO_4)_6F_2:Eu^{2+}$,[105] and 2419 cm^{-1} for $Sr_9Mg_{1.5}(PO_4)_7:0.06Eu^{2+}$,[106] the obtained fluoride blue phosphors $Ba_5Al_3F_{19}:0.005Eu^{2+}$ shows a better thermal stability. Considering that the operation temperature for the high-performance LEDs chips should be 100 - 150 °C (373 - 423 K), it could be suggested Eu^{2+}-doped $Ba_5Al_3F_{19}$ exhibits good thermal stability for its potential application.[107][108]

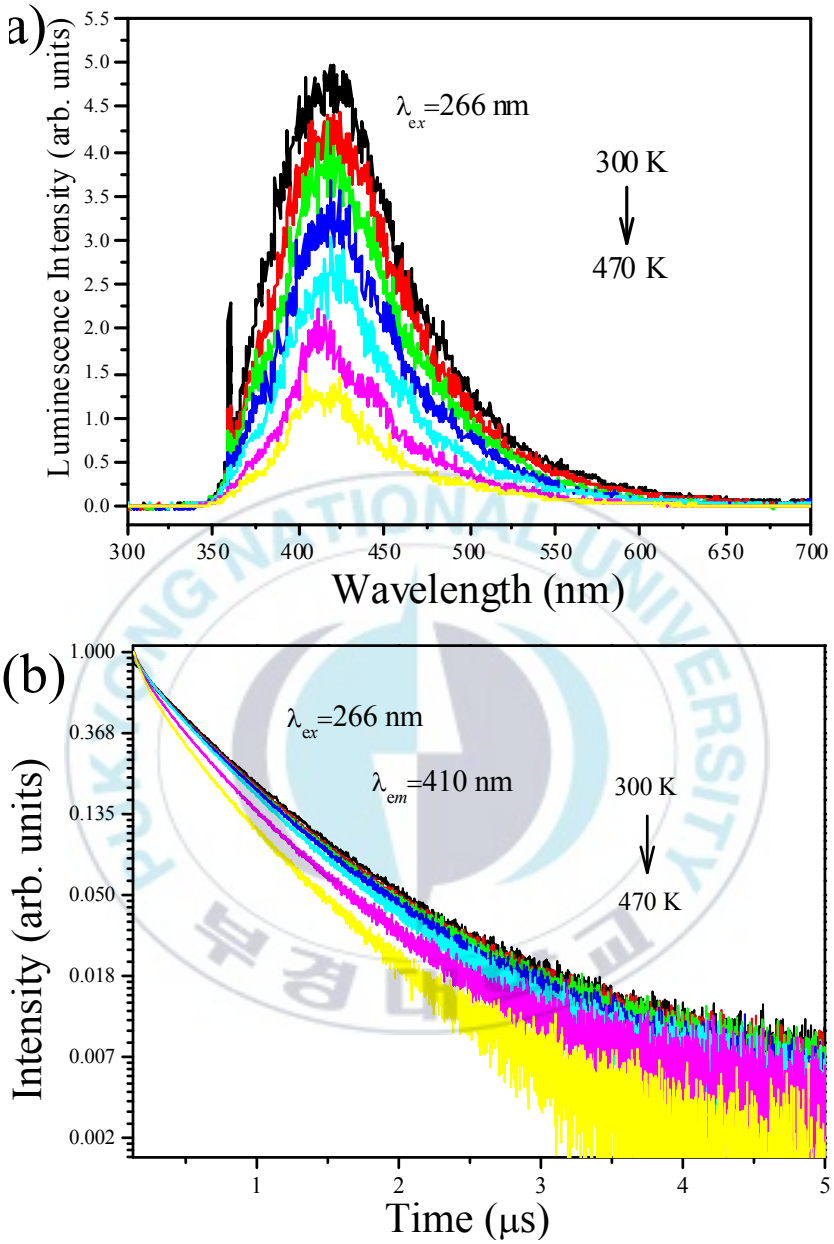

Fig. 4-8 Emission spectra (a) and decay curves (b) of $Ba_5Al_3F_{19}$:0.005Eu^{2+} excited by 266 nm laser with various temperatures ranging from 300 to 470 K. Colored lines means the emission spectra or decay curves at different temperature.

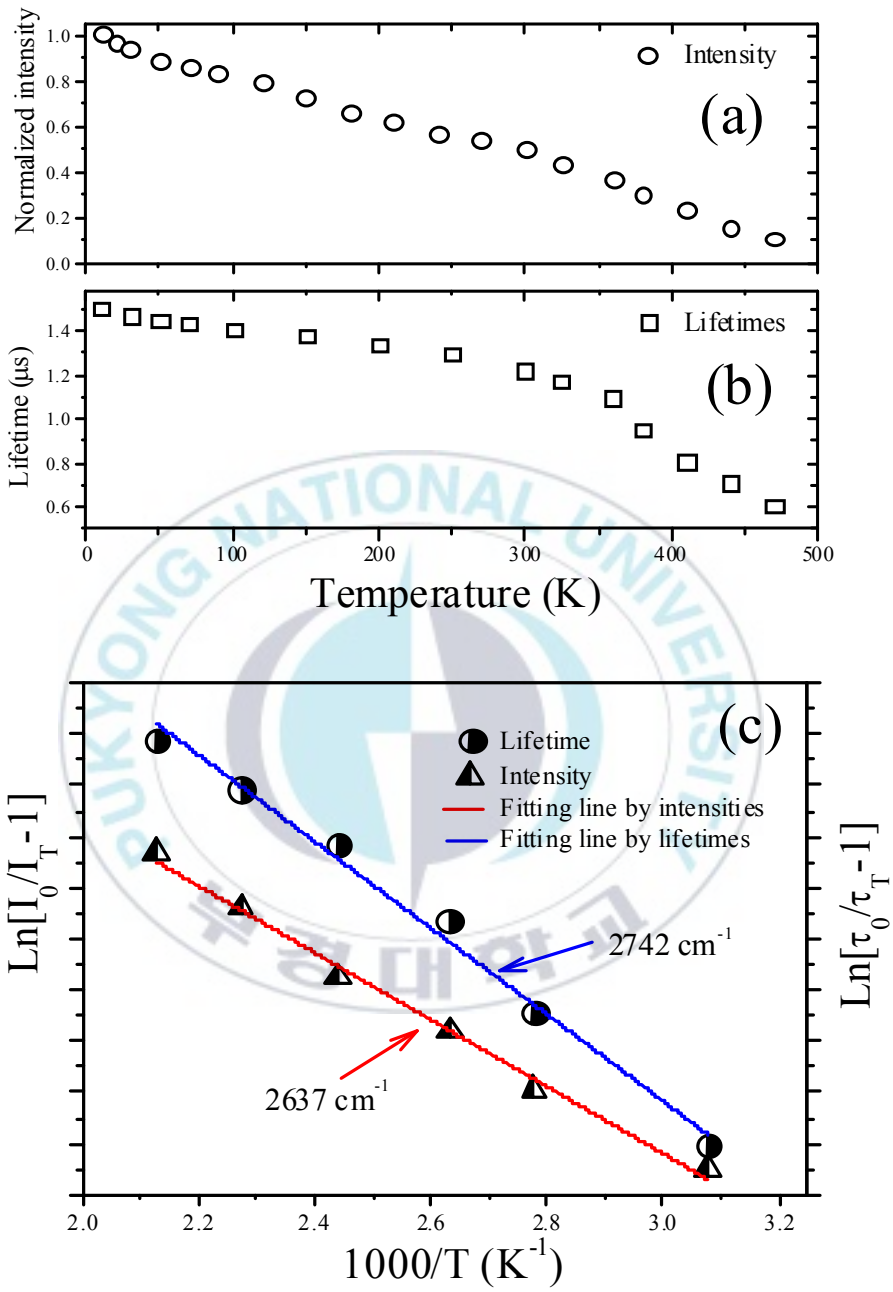

Fig. 4-9 Emission intensities (a) and decay times (b) as a function of temperature and the relationship (c) of $Ln[I_0/I_T-1]$ (red) and $Ln[\tau_0/\tau_T-1]$ (blue) with 1000/T for $Ba_5Al_3F_{19}:0.005Eu^{2+}$ based on (a) and (b).

5. Preparation, characterization and luminescent properties of red-emitting phosphor: $LiLa_2NbO_6$ doped with Mn^{4+} ions

5.1. Introduction

Recently, more attention has been paid to phosphors doped with transition metal ions with $3d^3$ electronic configuration. Typically, red-emitting Mn^{4+} is related to several vibrational sidebands, which are influenced by covalency and coordination symmetry. Therefore, optical properties of Mn^{4+} are closely related to the host matrix.[109] Generally, Mn^{4+} ions can only be accommodated and stabilized in an octahedral lattice site of the host crystals, such as including AlO_6, NbO_6, TiO_6, SiO_6, AlF_6, TiF_6, SiF_6, GeF_6 octahedron and so on, with broad absorption spectrum in the range of 220 - 600 nm and show red-emitting within the range 600 - 780 nm.[110]

As previously reported, Mn^{4+}-doped luminescence materials can be divided into two categories: Mn^{4+}-doped fluorides and Mn^{4+}-doped oxides. The Mn^{4+}-doped fluorides, e.g., K_2SiF_6, K_2TiF_6,[33] $BaGeF_6$,[111] usually show sharp red emission with peaks at around 630 nm. The Mn^{4+} luminescence in fluoride lattices has been patented for use in white light generating phosphor blends in LED devices.[3] While, Mn^{4+}-doped oxides, $CaAl_{12}O_{19}$,[112] $Ca_{14}Zn_6Al_{10}O_{35}$,[113] and $CaMg_2Al_{16}O_{27}$,[1] usually exhibit

deep red emission at around 700 nm. Such materials can be used as potential candidates for holographic recording and optical data storage,[114][115] laser application,[116] and thermoluminescence dosimetry.[117] Regretfully, fluoride hosts are unstable in environment. Moreover, the toxic HF solution used in the fluoride synthesis process is harmful to the environment. As an alternative, Mn^{4+}-activated oxides are more favorable because of their high chemical stability and ecofriendly preparation procedure. On the other hand, in the past few years, a large amount of novel Mn^{4+}-activated red emitting fluorides or oxides phosphors have been developed as mentioned above. However, few works focused on the luminescent mechanism of Mn^{4+} doped phosphors. To explore new kinds of candidates, more deep investigations on the luminescent mechanism are necessary.

The purpose of the current work is to provide a comprehensive study of the luminescence mechanism of the Mn^{4+} ion in the $LiLa_2NbO_6$ lattice with octahedral NbO_6 emitting center. In addition, Li congaing neonates are very sensitive to the intrinsic defects which may improve the optical properties of $LiLa_2NbO_6:Mn^{4+}$ red emitting phosphors.[118] $LiLa_2NbO_6:Mn^{4+}$ were synthesized via the solid state method, and then the luminescence properties are characterized in detail by temperature-dependent photoluminescence excitation, emission spectra and decay curves.

5.2. Results and discussion

5.2.1. Phase formation and crystal structure

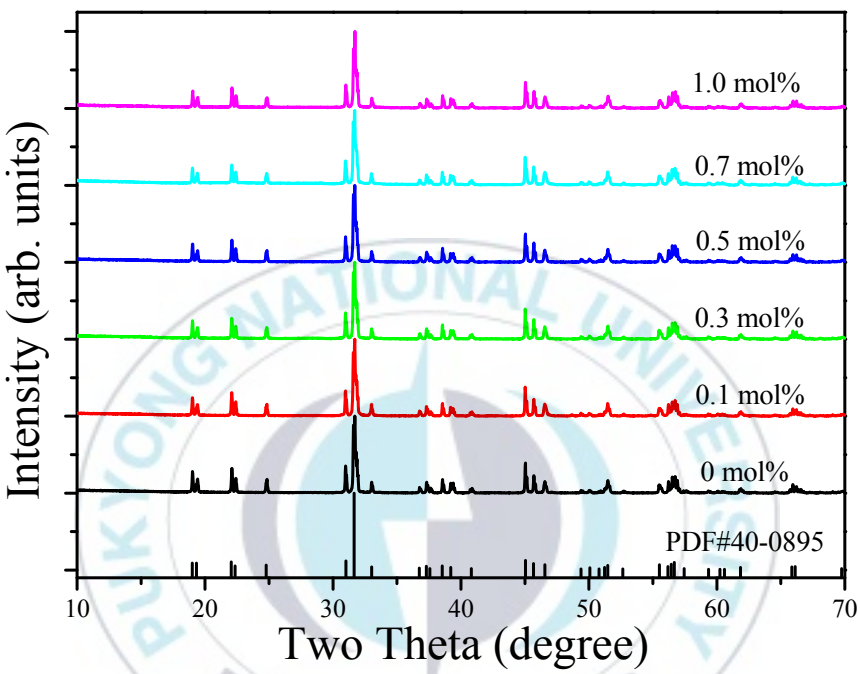

Fig. 5-1 the XRD patterns of $LiLa_2NbO_6:Mn^{4+}$ with different Mn^{4+} concentration. The standard pattern card PDF2 No.40-0895 is for comparison

Fig. 5-1 shows the XRD patterns of the $LiLa_2Nb_{1-x}Mn_xO_6$ ($0.005 \leq x \leq 0.01$) phosphors and the standard PDF card (JCPDS No. 40-0895). All the XRD patterns match well with the standard PDF card. The $LiLa_2NbO_6$ crystal is built up of alternating strands of LiO_6 and slightly disordered NbO_6 with La^{3+} locating in the cavities of the interconnected network.[119]

Based on requirements of the radius similarity and the charge balance between Nb^{5+} and Mn^{4+} (R_{Nb} = 0.64 nm and R_{Mn} = 0.54 nm for CN = 6), the Mn^{4+} ions substitute for the Nb^{5+} ions in the $LiLa_2NbO_6$ lattice.[55] The Mn^{4+} ions reside randomly in the sites of six coordinated Nb^{5+} ions to form the luminescence centers [MnO_6].

5.2.2. Luminescence characteristics of Mn^{4+} in $LiLa_2NbO_6$

The energy levels of the Mn^{4+} ($3d^3$) ions in a crystal could split into a number of sublevels depending on the crystal-field strength and symmetry. The splitting of the energy levels of Mn^{4+} in an octahedral crystal field can be described by the Tanabe-Sugano diagram of the d^3 electronic configuration,[32] as displayed in **Fig. 5-2a**. The doublet and quartet states are indicated by the red and the black, respectively. The energy levels in the Tanabe-Sugano diagram are strongly influenced by the local crystal field strength (D_q) except for the ^2E and $^2T_1$ states. Due to its high effective charge, the Mn^{4+} ion experiences a strong crystal field and therefore the ^2E state acts as the lowest excited state. The room temperature excitation and emission spectra of $LiLa_2NbO_6$:Mn^{4+} (0.7 mol%) are shown in **Fig. 5-2b**. In the excitation spectrum, two broad bands are observed with the maxima at 350 and 480 nm assigned to the spin-allowed $^4A_2 \rightarrow {}^4T_1$ and $^4A_2 \rightarrow {}^4T_2$ transitions, respectively. The two excitation bands indicate that the emission due to the $^2E \rightarrow {}^4A_2$ transition of Mn^{4+} in $LiLa_2NbO_6$ can be efficiently excited through UV to blue light. The 480 nm excitation band corresponding to the $^4A_2 \rightarrow {}^4T_2$ transition exhibits two dips at 477.7 nm and

489.5 nm. The existence of the two dips is attributed to the weak Fano anti-resonance, i.e., the reabsorption of the ^2E and ^2T states superimposed on the $^4A_2 \rightarrow {}^4T_2$ transition.[120] The feature was also observed in some Cr^{3+}-doped crystals with weak crystal field strength.[121][122] Typical absorption spectrum was measured as the pink dotted line shown in **Fig. 5-2b**. The absorption spectrum is consistent with the excitation spectrum, the broad band absorption around 39000 cm^{-1} is due to the absorption of $[NbO_6]$ octahedron and the other two broad band absorption attribute to the spin-allowed $^4A_2 \rightarrow {}^4T_1$ and $^4A_2 \rightarrow {}^4T_2$ transitions.[123] Compared with other red emitting phosphors doped by Eu^{3+}or Sm^{3+}, which show weak absorption peaks at about 400 nm or 460 nm because the 4*f*-4*f* absorption transitions are forbidden by the parity selection rule and its optical oscillator strength is small, $LiLa_2NbO_6:Mn^{4+}$ with high absorption efficiency can be used as potential candidates.[124]

The emission spectrum exhibits the narrow band at around 712 nm corresponding to the parity- and spin-forbidden $^2E \rightarrow {}^4A_2$ transition. The emission of Mn^{4+} in $LiLa_2NbO_6$ has a full width at half-maximum (FWHM) of 40 nm which is narrower than that of the other Mn^{4+} doped oxide phosphors, for examples, 55 nm for Li^+ co-doped $SrMgAl_{10}O_{17}:Mn^{4+}$ red emitting phosphors[125] and 105 nm for $Na_2MgAl_{10}O_{17}:Mn^{4+}$ red emitting phosphors.[126] The narrow band is beneficial for improving the luminous efficiency of the radiation, color rendition, and visual energy efficiency.[127]

The luminescence characteristics of Mn^{4+} in $LiLa_2NbO_6$ are different from Mn^{4+}-doped fluoride hosts, which usually exhibit sharp emission lines

peaking at around 630 nm, like $Na_2SiF_6:Mn^{4+}$ and $BaGeF_6:Mn^{4+}$ et. al.[4][128] The large difference in the line position of the ^2E - $^4A_2$ emission between the fluoride and oxide hosts is due to the weaker nephelauxetic effect for the fluorides than for the covalent oxides, resulting in the higher emitting ^2E_g level position in fluoride than in oxides.[129]

The crystal-field strength (10Dq), two Racah parameters B and C of Mn^{4+} in the $LiLa_2NbO_6$ host can be determined by the following equations based on the excitation and emission spectra:[130]

$$D_q = E(^4A_{2g} - {}^4T_{2g})/10 \quad \textbf{(5-1)}$$

$$\frac{D_q}{B} = 15(x-8)/(x^2-10x) \quad \textbf{(5-2)}$$

$$\frac{E(^2E_g - {}^4A_{2g})}{B} = \frac{3.05C}{B} + 7.9 - \frac{1.8B}{D_q} \quad \textbf{(5-3)}$$

$$x = \frac{E(^4A_{2g} - {}^4T_{1g}) - E(^4A_{2g} - {}^4T_{2g})}{D_q} \quad \textbf{(5-4)}$$

$E(^4A_{2g}-{}^4T_{2g})$ refer to the peak energy (15152 cm^{-1}) for the $^4A_{2g}\rightarrow{}^4T_{2g}$ transition of Mn^{4+}, similarly, $E(^2E_g\rightarrow{}^4A_{2g})$ refer to the peak energy (15152 cm^{-1}) for the $^2E_g\rightarrow{}^4A_{2g}$ transition of Mn^{4+} and $E(^4A_{2g}\rightarrow{}^4T_{2g})$ refer to the peak energy (15152 cm^{-1}) for the $^4A_{2g}\rightarrow{}^4T_{2g}$ transition of Mn^{4+}. From **Eqs. (5-1)-(5-4)**, the crystal field parameters Dq, B, and C are calculated to be 2081, 719, and 2895 cm^{-1}, respectively. Dq/B is estimated to be 2.89 as described in **Fig. 5-2a** by the red arrow, indicating that the Mn^{4+} ions in $LiLa_2NbO_6$ experience stronger crystal-field strength than those in

fluorides (for example, $Na_2SiF_6:Mn^{4+}$: Dq=2174 cm^{-1}, B=775 cm^{-1}, C=3475 cm^{-1}, Dq/B = 2.805).[73]

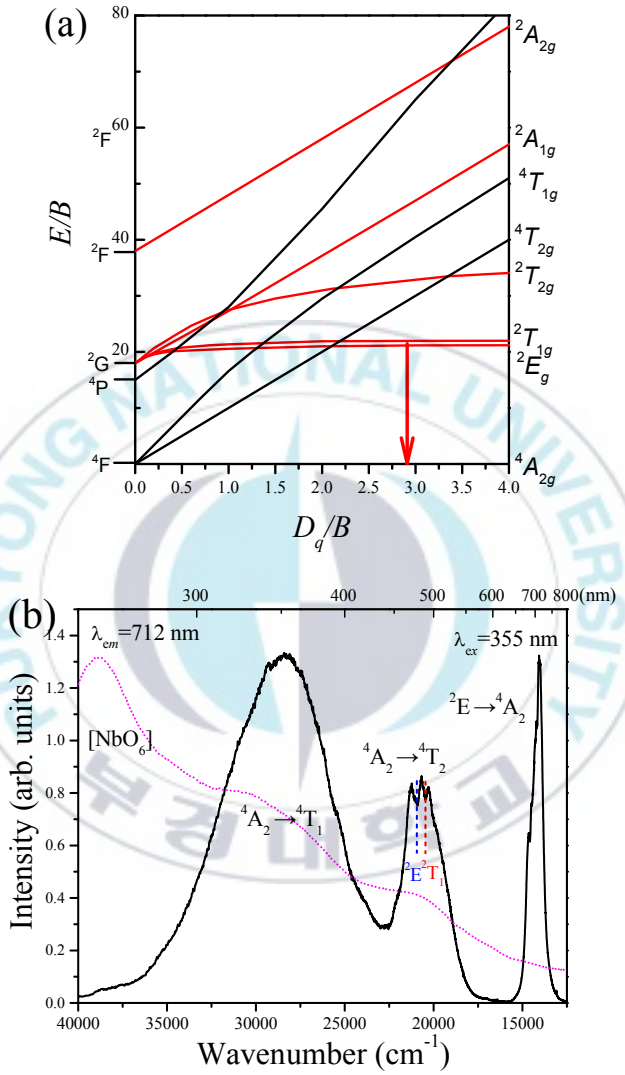

Fig. 5-2 (a) The Tanabe-Sugano energy-level diagram for d^3 ions. (b) Typical excitation, emission and absorption spectra of $LiLa_2NbO_6$:0.7%Mn^{4+} phosphor.

5.2.3. Concentration dependent luminescence proprieties of Mn^{4+} in $LiLa_2NbO_6$ lattice

Figs. 5-3a and **5-3b** show the excitation and emission spectra of $LiLa_2NbO_6:Mn^{4+}$ as functions of Mn^{4+} concentration, respectively. The emission and excitation intensities of $LiLa_2NbO_6:Mn^{4+}$ increase with increasing Mn^{4+} concentration until the concentration reaches 0.7 mol%, and then decreases due to the concentration quenching. The concentration quenching occurs by the energy transfer within the nearest Mn^{4+} ions, and ends with energy transfer to traps or killer sites.[131][132] Usually, the critical quenching concentration of the Mn^{4+}-doped phosphors is lower than that in rare-earth doped phosphors, because the interaction in rare-earth doped phosphors is weaker in the view of the well-shielded 4*f* electrons.[133]

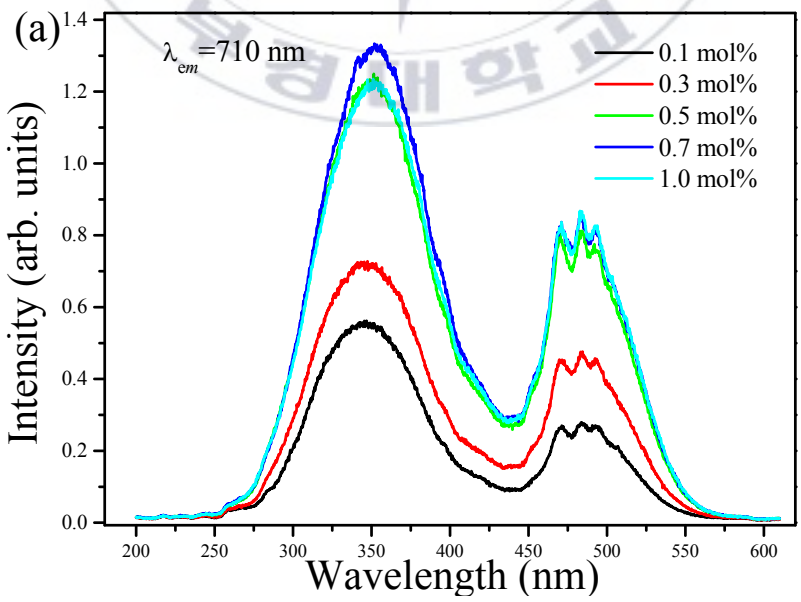

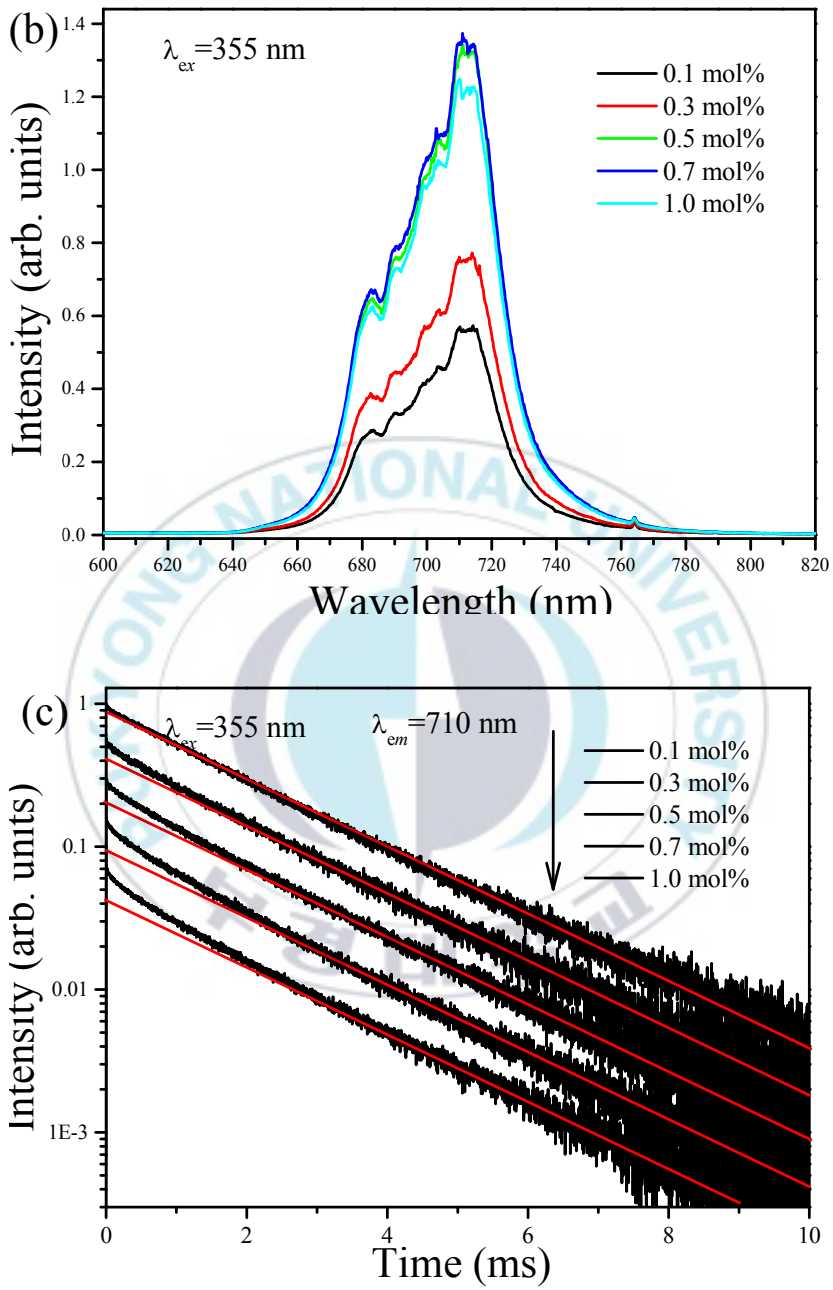

Fig. 5-3 Room temperature excitation (a), emission spectra (b) and decay curves (c) of $LiLa_2NbO_6:Mn^{4+}$ with different Mn^{4+} concentration.

The decay curves of $LiLa_2NbO_6$:$x$$Mn^{4+}$ with different Mn^{4+} concentrations at room temperature are shown in **Fig. 5-3c**. The decays are nonexponential and fast in the initial stage and then overall single exponential in late times. The room temperature decay times for all the concentrations are estimated to be about 1.75 ms except for the initial stage. The single exponential decays with the same decay times in the Mn^{4+} concentration of 0.1 - 1.0 mol% may imply that only a single emission center $Nb(Mn)O_6$ forms in the $LiLa_2NbO_6$ lattice. However, the nonexponential decays at initial stages depend on the Mn^{4+} concentration. The deviation from the single exponential is gradually larger with increasing Mn^{4+} concentration. The nonexponential decays are attributed to the fast energy transfer from Mn^{4+} to other defect centers (killer centers) or other Mn^{4+} ions nearby.[134] The larger formation of defect centers in $LiLa_2NbO_6$:Mn^{4+} are responsible for the larger deviation from the single exponential with increasing Mn^{4+} concentration.

5.2.4. Vibrational structure and thermal quenching of the Mn^{4+} $^2E_g \rightarrow {}^4A_{2g}$ luminescence

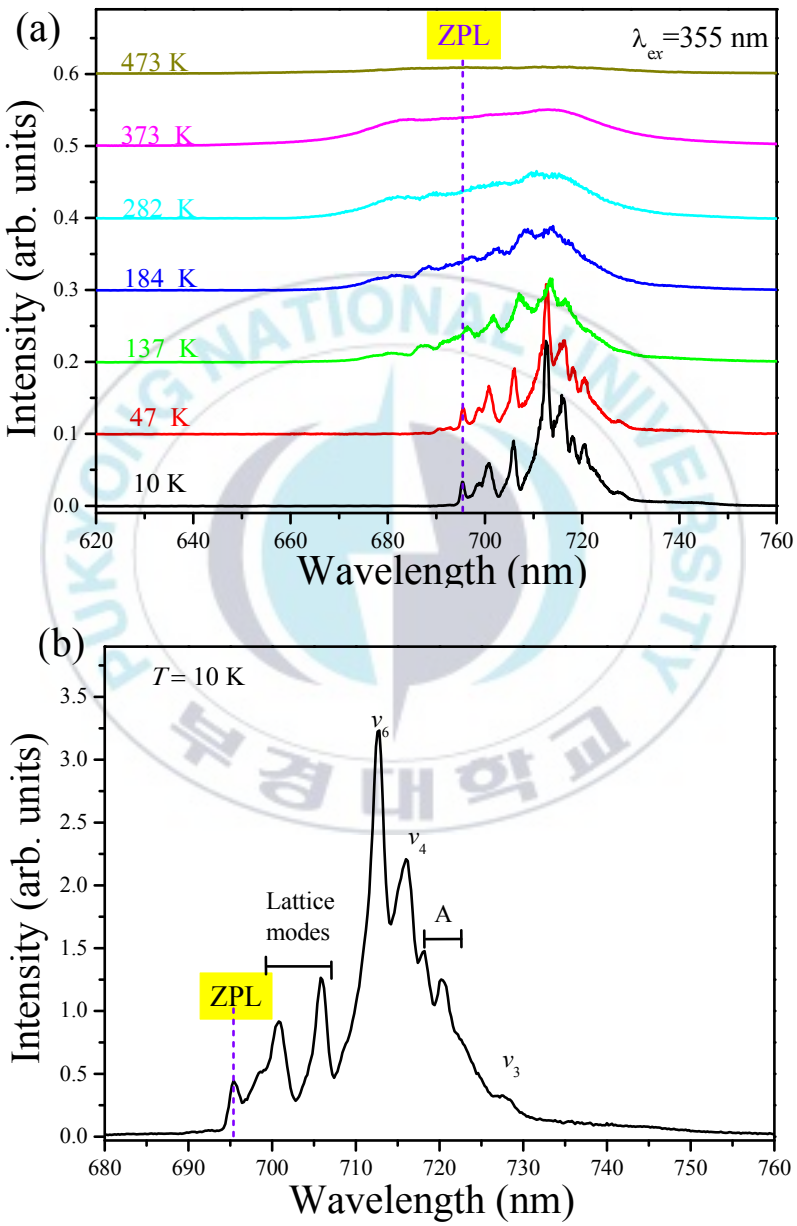

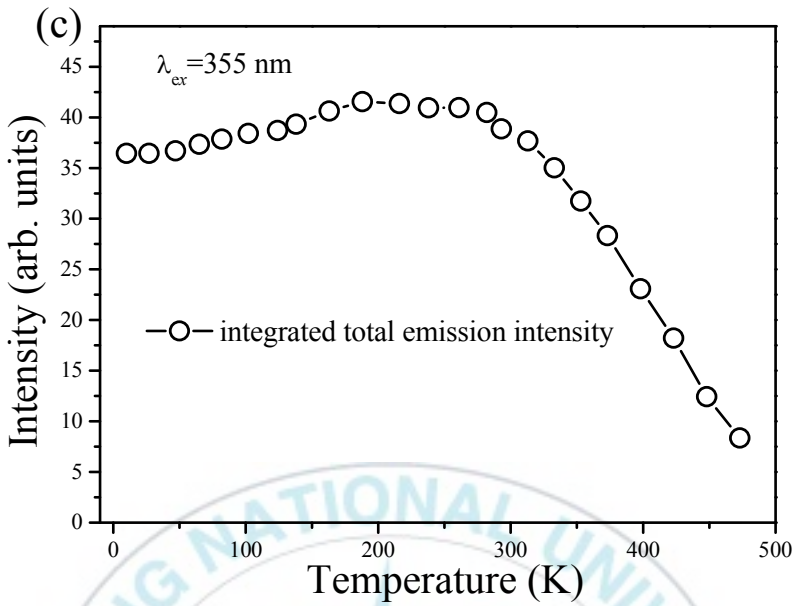

Fig. 5-4 Temperature dependent emission spectra (10-480 K) (a), emission spectrum of $LiLa_2NbO_6$:0.7%Mn^{4+} at 10 K (b), and integrated emission intensities (c) due to the $^2E_g \rightarrow {}^4A_{2g}$ transition as a function of temperature for $LiLa_2NbO_6$:0.7%Mn^{4+}.

Fig. 5-4a shows the emission spectra of $LiLa_2NbO_6$:Mn^{4+} (0.7 mol%) at various temperatures (10-480 K). Different spectral features are observed at different temperatures. Several luminescence characteristics can be observed:

(1) With increasing temperature, the emission lines become broader and appear not only on the low-energy side but also on the high-energy side of zero-phonon line (ZPL) at 695.5 nm (14380 cm^{-1}), which are known as the Stokes and anti-Stokes emissions, respectively. The broaden of

the emission attribute to two parts. Firstly, the contribution of the electron-phonon subsystems will result in the spectral broadening of the corresponding emissions pectra. At low temperature, the influence of phonon subsystem is low, however, with increasing the temperature, the influence of the phonon subsystem increased, which will result in the broaden of the emission spectra.[135] In addition, at low temperature, the energy states of Mn^{4+} are more likely to be distributed in the vibrational ground state and therefore Stokes emission primarily occurs. However, when temperature increases, electrons have enough energy to populate the upper vibrational states and relax back to the ground state of $^4A_2$ with the anti-Stokes emission.[67]

(2) The ZPL observed at 695.5 nm (14380 cm^{-1}) has weak intensity relative to the vibrational emission lines because the zero-phonon transition is forbidden for electric dipole radiation due to the inversion symmetry of the D_{3d} site.[136] The appearance of the ZPL beyond 650 nm is typical in oxide lattices, for instance, α-$LiAlO_2$:Mn^{4+} (656 nm),[137] $SrTiO_3$:Mn^{4+} (723 nm),[138] and La_2MgTiO_6:Mn^{4+} (687 nm).[139] The ZPL of 695.5 nm in $LiLa_2NbO_6$:Mn^{4+} is well beyond 650 nm due to a large nephelauxetic effect as discussed above. However, the Mn^{4+} ions in fluorides prefer the energy of the emitting $^2E \rightarrow {}^4A_2$ transition with a ZPL in the 617 -624 nm range.[140][141]

(3) **Fig. 5-4b** shows the emission spectrum of LiLa2NbO6:0.7%Mn^{4+} at 10 K. According to the group theory, there are six vibrational modes for an octahedron with O_h symmetry: υ_1 (A_{1g}), υ_2 (E_g), υ_3 (T_{1u}), υ_4 (T_{1u}),

υ_5 (T_{2g}) and υ_6 (T_{2u}).[142][143] The most intense vibrational $^2E \rightarrow {}^4A_2$ emission lines at 712 and 716 nm are assigned to the υ_6 mode (~350 cm^{-1} relative to the ZPL) and υ_4 mode (~420 cm^{-1} relative to the ZPL) of the MnO_6 octahedron, respectively. The weak emission peak at around 728 nm (13730 cm^{-1}) is assigned to the υ_3 vibrational mode of the MnO_6 octahedron which is usually located at the energy of ~650 cm^{-1} relative to the ZPL.

(4) **Fig. 5-4c** shows the total integrated emission intensities of the $^2E \rightarrow {}^4A_2$ transition as a function of temperature from 10 to 480 K. Note that the integrated emission intensity increases slightly up to about 300 K compared with the initial intensity at 10 K and then decreases due to the intense nonradiative transition rate. Usually, the emission intensity of a certain luminescent phosphor consistently decreases with increase in temperature which is mainly due to the increase of the nonradiative transition rate.[1] Here, the initial elevation may be caused by the thermal population of higher vibrational states resulting in the increase of the anti-Stokes sideband, which compensates and overtakes the intrinsic thermal quenching effect.[144] With further increase in temperature, the influence of nonradiative transition at elevated temperature becomes dominant leading to decrease in the emission intensity.

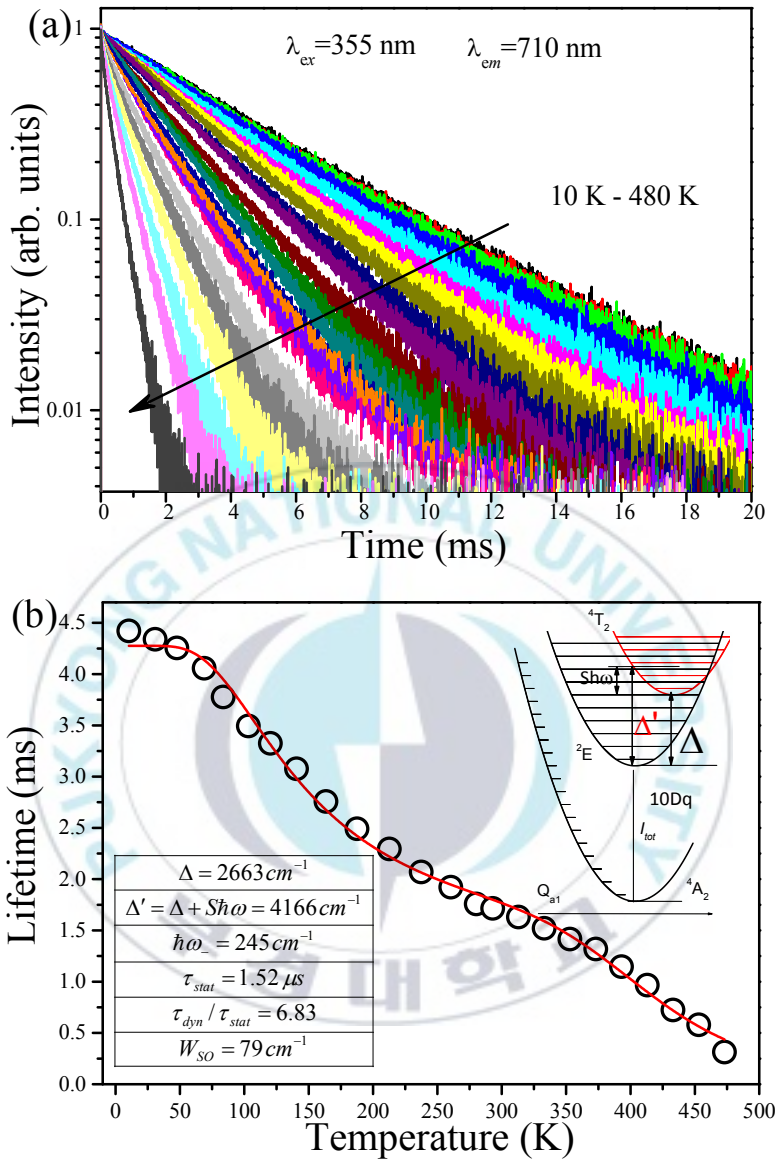

Fig. 5-5 (a) Temperature dependent decay curves as a function of temperature (10 - 480 K) (b) Decay times of the ^2E_g state as a function of temperature (10-480 K) for $LiLa_2NbO_6$:0.7%Mn^{4+}. The inset of (b) is configuration coordinate diagram of Mn^{4+} including the ground state and the lowest excited states without spin-orbit interaction.

Fig. 5-5a shows decay curves of the 712 nm ^2E emission under the excitation of 355 nm in the temperature range 10 - 480 K. The decays are single exponential and shorten monotonically from 4.4 ms (10 K) to 0.44 ms (480 K). The decay times as a function of temperature are shown in **Fig. 5-5b.**

The temperature dependent decay times of Mn^{4+} can be analyzed by the model for Cr^{3+} suggested by Grinberg. Cr^{3+} is isoelectronic with Mn^{4+} ($3d^3$ configuration). According to this model, an additional relaxation pathway (the spin-allowed $^4T_2 \rightarrow {}^4A_2$ transition) occurs with increasing temperature and the temperature dependent decay times can be written by the following equation.

$$\tau = \frac{\tau_{stat}\left(1+\exp\left(-\frac{\hbar\omega_-}{kT}\right)+3\exp\left(-\frac{\Delta}{kT}\right)\right)}{\left(1+\frac{\tau_{stat}}{\tau_{dyn}}\exp(-\frac{\hbar\omega_-}{kT})\right)\left(\left(\frac{W_{so}}{\Delta'}\right)^2+3\exp\left(-\frac{\Delta}{kT}\right)\right)} \quad \textbf{(5-5)}$$

where Δ' represents the energy difference between the ^2E and $^4T_2$ states which can be calculated from the excitation spectrum and Δ is the energy difference between the minimum energy of the ^2E and $^4T_2$ states. $\hbar\omega_-$ is considered as a free parameter for the effective energy of phonons and W_{SO} is an average spin-orbit parameter. $\frac{\tau_{stat}}{\tau_{dyn}}$ is the ratio of the radiative decay times induced by static and dynamic processes. In addition, $\frac{1}{\tau_{dyn}}$ is explicitly independent on temperature.[33]

The temperature dependent decay times are fitted with **Eq. (5-5)** and

the best fit results are shown on **Fig. 5-5b**. The results are Δ'=4166 cm^{-1}, Δ= 2663 cm^{-1}. $\hbar\omega$ = 245 cm^{-1}, W_{SO} = 79 cm^{-1}, τ_{stat} = 1.52 μs and $\frac{\tau_{dyn}}{\tau_{stat}}$ =6.83. The results indicate that an additional relaxation pathway (the spin-allowed $^4T_{2g} \rightarrow {}^4A_{2g}$ transition) due to the spin-orbit interaction of the ^2E_g and $^4T_{2g}$ states occurs with increasing temperature. The radiative lifetime τ_{stat} (1.52 μs) related to the $^4T_{2g} \rightarrow {}^4A_{2g}$ transition is much shorter than the observed $^2E_g \rightarrow {}^4A_{2g}$ transition. Therefore, it is hard to identify the emission from the spin-allowed $^4T_{2g} \rightarrow {}^4A_{2g}$ transition. The fit result of $\frac{\tau_{dyn}}{\tau_{stat}}$ indicates that the appearance of anti-Stocks sideband causes increase in the spin-forbidden $^2E_g \rightarrow {}^4A_{2g}$ transition about 6.83 times.

6. Conclusions

In this work, several high efficient phosphors have been prepared and the luminescence properties were confirmed by experiment results.

In chapter 3, the $Ba_5AlF_{13}:Mn^{4+}$ nanoparticles were developed by the two-step coprecipitation method. The well-crystallized particles were obtained with the size ranging from 300 to 500 nm. The phosphors can be effectively excited by near UV - blue light and show bright red emitting colors with the several sharp line emissions in the wavelength region 600 - 660 nm. An intense ZPL emission at 620 nm is observed even at room temperature, which can be attributed to the incorporation of Mn^{4+} ions on highly distorted octahedral lattice sites. The temperature dependent luminescence indicates that the $Ba_5AlF_{13}:Mn^{4+}$ red phosphor shows special anti-thermal quenching behavior by comparison with its emission intensity at 300 K relative to 10 K. In addition, according to the temperature dependent decay curves, a modified dynamic model was employed indicating an additional relaxation pathways (the spin-allowed $^4T_{2g} \rightarrow {}^4A_{2g}$ transition) occurs with increasing temperature.

In chapter 4, a series of $Ba_5Al_3F_{19}:Eu^{2+}$ phosphors were prepared via a solid state reaction. The blue-emitting $Ba_5Al_3F_{19}$: Eu^{2+} phosphors can be well excited by the UV to blue light and exhibit a wide emission band covering from 350 to 600 nm ascribed to the *d-f* transition of Eu^{2+} ions. The sharp line peaked at 360 nm originates from the *f-f* transition of the Eu^{2+} is also observed which shows a longer decay time of 0.54 ms at 10 K. The

thermal quenching effect of $Ba_5Al_3F_{19}:Eu^{2+}$ phosphors were evaluated by measuring the temperature dependent emission spectra and decay curves. $Ba_5Al_3F_{19}:Eu^{2+}$ phosphors show high thermal stability (ΔE= 2637 cm^{-1}) compared with some reported oxides blue phosphors. The excellent thermal properties demonstrate that $Ba_5Al_3F_{19}:Eu^{2+}$ phosphors have great potential to serve as promising blue-emitting phosphor candidates.

In chapter 5, we investigate the luminescence properties of $LiLa_2NbO_6:Mn^{4+}$ red emitting phosphors in the temperature range 10 - 480 K. The obtained spectroscopic properties are compared with the Mn^{4+} in other oxides and fluorides. Concentration dependent excitation and emission spectra were measured and the optimum doping concentration of Mn^{4+} in $LiLa_2NbO_6$ lattice was 0.7 mol%. It's worth noting that the sharp emission lines corresponding to the local vibrational modes of Mn^{4+} ions in the $LiLa_2NbO_6$ lattice are observed in low temperature. Otherwise, the $LiLa_2NbO_6:Mn^{4+}$ red emitting phosphors shows unusual anti-thermal quenching behavior, i.e., the integrated total emission intensities increase slightly and then decrease due to the thermal quenching effect. The luminescence decays of the Mn^{4+} ^2E state as functions of temperature are investigated. A modified dynamic model was employed to deeply investigate the temperature dependent decay times. The result indicates that an additional relaxation pathway (the spin-allowed $^4T_2 \rightarrow {}^4A_2$ transition) occurs with increasing temperature. We demonstrate that the $LiLa_2NbO_6:Mn^{4+}$ can be used as potential red emitting phosphors.

Acknowledgements

It is a significant and unforgettable experience for me to spend such a long time on writing, modifying and polishing this thesis. Many kind-hearted people give me a great amount of help, professional advice and encouragement. Thus, here I would like to express my sincere gratitude to them.

First of all, I will show my sincere thanks to my supervisor Professor Hyo Jin Seo, who always give me invaluable guidance and constant support and encouragement throughout the doctoral career. During my study of professional knowledge in my all doctoral career and the witting of this thesis, he has always been generous to offer me useful suggestions answer my questions and discuss research questions with me. His detail guidance and helpful comments encourage me to overcome all difficulties and think more critically.

I will also express my sincere gratitude to Professor Yanlin Huang from Soochow University, China, who always give me constructive suggestion to my thesis and thanks to him for instructing me to construct my professional knowledge in the past six years.

I want to thank all my affectionate lab mates and friends, Peiqing Cai, Han Cheng, Jing Wang, Shala Bi, Fanfan Zhu, Cuili Chen, Jing Li. During the three years' learning and living, they always give me a lot of support and encouragement in their own ways.

At last, I will give the deepest gratitude to my family for their

regretless support and love to me. Special thanks to my dear parents and relative of concern, understanding and support, over the three years, they silently support with my studies and growth enabled me to come fully into the doctoral career!

Finally, I sincerely wish all of you happiness and happiness!

References

[1]W. J. Par, Y. H. Song, J. W. Moon, S. M. Kang, D. H. Yoon, Solid State Sci. **12**, 1853 (2010).

[2]Y. Q. Li, A. C. A. Delsing, G. de With, H. T. Hintzen, Chem. Mater. **17**, 3242 (2005).

[3]Y. Uchida, T. Taguchi, Opt. Eng. **44**, 124003 (2005).

[4] R. Mueller-Mach, G. Mueller, M. R. Krames, H. A. Höppe, F. Stadler, W. Schnick, T. Juestel, P. Schmidt, Phys. status solid **202**, 1727 (2005).

[5] R. Mueller-Mach, G. O. Mueller, M. R. Krames, T. Trottier, IEEE J. Sel. Top. Quantum Electron. **8**, 339 (2002).

[6]S. Nakamura, G. Fasol, **1**, 216 (1997).

[7]E. S. Zolotova, M. I. Rakhmanova, V. V. Sokolov, E. M. Uskov, Inorg. Mater. **47**, 1249 (2011).

[8] Z. Y. Lin, X. L. Liang, Y. W. Ou, C. X. Fan, S. L. Yuan, H. D. Zeng, G. R. Chen, J. Alloys Compd. **496**, L33 (2010).

[9] L. Zhou, J. Wei, J. Wu, F. Gong, L. Yi, J. Huang, J. Alloys Compd. **476**, 390 (2009).

[10] C. F. Guo, Y. Xu, F. Lv, X. Ding, J. Alloys Compd. **497**, L21 (2010).

[11] T. Nishida, T. Ban, N. Kobayashi, Appl. Phys. Lett. **82**, 3817 (2003).

[12] X. D. Qi, C. M. Liu, C. C. Kuo, J. Alloys Compd. **492**, L61 (2010).

[13] C. H. Liang, Y. C. Chang, Y. S. Chang, Appl. Phys. Lett. **93**, 211902 (2008).

[14] D. R. Gamelin, H. U. Güdel, Acc. Chem. Res. **33**, 235 (2000).

[15] T. Aitasalo, P. Dereń. J. Hölsä, H. Jungner, J.C. Krupa, M. Lastusaari. J. Legendziewicz, J. Niittykoski, W. Stręk, J. Solid State Chem. **171**, 114

(2003).

[16] G. Tyler, Plant and Soil **267**, 191 (2004).

[17] J. M. F. van Dijk, M. F. H. Schuurmans, J. Chem. Phys. **78**, 5317 (1983).

[18] J. C. Krupa, M. Queffelec, J. Alloys Compd. **20**, 287 (1997).

[19] R. Grasser, A. Scharmann, K. R. Strack, J. Lumin. **27**, 263 (1982).

[20] A. Mills, III-Vs Review **1**, 32 (2005).

[21] M. H. Li, L. L. Wang, W. G Ran, Z. H Deng, J. S. Shi, C. Y. Ren, Materials **10**, 227 (2017).

[22] R. Debnath, A. Nayak, A. Ghosh, Chem. Phys. Lett. **444**, 324 (2007).

[23] X. Q. Piao, K. I. Machida, T. Horikawa, H. Hanzawa, Y. Shimomura, N. Kijima, Chem. Mater. **19**, 4592 (2007).

[24] D. Wilhelm, D. Baumann, M. Seibald, K. Wurst, G. Heymann, H. Huppertz, Chem. Mater. **29**, 1204 (2017).

[25] L. Brewer, J. Opt. Soc. Am. **61**, 1666 (1971).

[26] G. K. Liu, Electronic energy level structure, in: G.K. Liu, B. Jacquier (Eds.), Springer 2005.

[27] P. Dorenbos, J. Lumin. **21**, 91 (2000).

[28] J. R. Oh, S. H. Cho, Y. H. Lee, Y. R. Do, Optics Express **17**, 7450 (2009).

[29] Y. Shimizu, K. Sakano, Y. Noguchi, T. Moriguchi, U.S. Patent # **5**, 998 (1999).

[30] B. Wang, H. Lin, J. Xu, H. Chen, Y. S. Wang, ACS appl. Mater. Inter. **6**, 22905 (2014).

[31] K. Li, H. Z. Lian, R. V. Deuna, J. Lumin. **198**, 155 (2018).

[32] Y. Tanabe, S. Sugano, J. Phys. Soc. Jpn. **9**, 776 (1954).

[33] H. M. Zhu, C. C. Lin, W. Q. Luo, S. T. Shu, Z. G. Liu, Y. S. Liu, J. T. Kong, E. Ma, Y. G. Cao, R. S. Liu, X. Y. Chen, Nat. Commun. **5**, 4312 (2014).

[34] H. G. Kang, J. K. Park, C. H. Kim, S. C. Choi, J. Ceram. Soc. Jap. **117**, 647 (2009).

[35] M. M. Shang, J. Wang, J. Fan, H. Z. Lian, Y. Zhang, J. Lin, J. Mater. Chem. C **3**, 9306 (2015).

[36] G. Blasse, B. C. Grabmaier, Luminescent Materials; Spring-Verlag: Berlin, 1994.

[37] D. T. Palumbo, J. J. Brown, J. Electrochem. Soc. **117**, 1184 (1970).

[38] D. T. Palumbo, J. J. Brown, J. Electrochem. Soc. **118**, 1159 (1971).

[39] J. Zhao, C. F. Guo, X. Y. Su, H. M. Noh, J. H. Jeong, J. Am. Ceram. Soc. **97**, 1878 (2014).

[40] L. Wu, B. Wang, Y. Zhang, L. Li, H. R. Wang, H. Yi, Y. F. Kong, J. J. Xu, Dalton T. **43**, 13845 (2014).

[41] P. Du, L. K. Bharat, X. Y. Guan, J. S. Yu, J. Appl. Phys. **117**, 083112 (2015).

[42] C. J. Duan, A. C. A. Delsing, H. T. Hintzen, Chem. Mater. **21**, 1010 (2009).

[43]X. Y. Huang, Nat. Photonics **28**, 748 (2014).

[44]J. K. Sheu, F. B. Chen, Y. C. Wang, C. C. Chang, S. H. Huang, C. N. Liu, M. L. Lee, Opt. Express **7**, A232 (2015).

[45] J. C. Boyer, F. Vetrone, L. A. Cuccia, J. A. Capobianco, J. Am. Chem. Soc. **128**, 7444 (2006).

[46] Y. G. Su, L. P. Li, G. S. Li, Cryst Growth Des. **8**, 2678 (2008).

[47] H. Bode, H. Jenssen, F. Bandte, Angew. Chem. Int. Edit. **65**, 304 (1953).

[48] A. Kozak, M. Samouël, J. Renaudin, G. Ferey, Anorg. Allg. Chem. **613**, 98 (1992).

[49] T. Grzyb, A. Szczeszak, Z. Śniadecki, B. Idzikowski, S. Lis, J. Alloys Compd. **686**, 489 (2016).

[50] Z. L. Wang, N. Wang, Z. Y. Yang, Z. F. Yang, Q. W. Wei, Q. Zhou, H. B. Liang, Journal of. Lumin. **192**, 690 (2017).

[51] L. Huang, Y. W. Zhu, X. J. Zhang, R. Zou, F. J. Pan, J. Wang, and M. M. Wu, *Chem. Mater.* **28**, 1495 (2016).

[52] L. L. Wei, C. C. Lin, Y. Y. Wang, M. H. Fang, H. Jiao, R. S. Liu, ACS Appl. Mater. Inter. **7**, 10656 (2015).

[53] T. Han, T. C. Lang, J. Wang, M. J. Tu, L. L. Peng. RSC Adv. **5**, 100054 (2015).

[54] C. Martineau, M. Allix, M. R. Suchomel, F. Porcher, F. Vivet, C. Legein, M. Body, D. Massiot, F. Taulelle, F. Fayon, Dalton T. **45**, 15565 (2016).

[55] R. D. Shannon, *Acta Crystallogr. A* **32**, 751 (1976).

[56] B. Henderson, G. F. Imbusch, Optical Spectroscopy of Inorganic Solids, Oxford University Press (1989).

[57] A. Lempicki, L. Andrews, S. J. Nettel, B. C. McCollum, E. I. Solomon, Phys. Rev. Lett. **44**, 1234 (1980).

[58] Y. Jin, M. H. Fang, M. Grinberg, S. Mahlik, T. Lesniewski, M. G. Brik, G. Y. Luo, J. G. Lin, R. S. Liu, ACS Appl. Mater. Inter. **8**, 11194 (2016).

[59] D. Sekiguchi, S Adachi, ECS J. Solid State Soc. **3**, R60 (2014).

[60] M. H. Fang, H. D. Nguyen, C. C. Lin, R. S. Liu, J. Mater. Chem. C **3**, 7277 (2015).

[61] M. G. Brika, S. J. Camardello, A. M. Srivastava, N. M. Avram, A. Suchocki, ECS J. Solid State Soc., **5**, R3067 (2016).

[62] L. L. Wei, C. C. Lin, M. H. Fang, M. G. Brik, S. F. Hu, H. Jiao and R. S.

Liu, *J. Mater. Chem. C* **3**, 1655 (2015).

[63] M. Y. Peng, X. W. Yin, P. A. Tanner, C. Q. Liang, P. F. Li, Q. Y. Zhang, J. R. Qiu, J. Am. Chem. Soc. **96**, 2870 (2013).

[64] Y. H. Jin, Y. R. Fu, Y. H. Hu, L. Chen, H. Y. Wu, G. F. Ju, M. He, T. Wang, Powder Technol. **292**, 74 (2016).

[65] R. P. Cao, Y. J. Ye, Q. Y. Peng, G. T. Zheng, H. Ao, J. W. Fu, Y. M. Guo, B. Guo, Dyes Pigments **146**, 14 (2017).

[66] D. Sekiguchi, J. Nara, S. Adachi, J. Appl. Phys. **113**, 183516 (2013).

[67] W. L. Wu, M. H. Fang, W. L. Zhou, T. Lesniewski, S. Mahlik, M. Grinberg, M. G. Brik, H. S. Sheu, B. M. Cheng, J. Wang, R. S. Liu, Chem. Mater. **29**, 935 (2017).

[68] X. D. Yi, R. F. Li, H. M. Zhu, J. Gao, W. W. You, Z. L. Gong, W. Guo, X. Y. Chen, J. Mater. Chem. C **6**, 2069 (2018).

[69] L. Y. Wang, E. H. Song, Y. Y. Zhou, T. T. Deng, S. Ye, Q. Y. Zhang, J. Mater. Chem. C **5**, 7253 (2017).

[70] T. T. Deng, E. H. Song, J. Sun, L. Y. Wang, Y. Deng, S. Ye, J. Wang, Q. Y. Zhang, J. Mater. Chem. C **5**, 2910 (2017).

[71] H. Jia, L. Cao, Y. Wei, H. Q. Wang, H. Xiao, G. G. Li, J. Lin, J. Alloys Compd. **738**, 307 (2018).

[72] M. Cheng, X. X. Wu, W. C. Zheng, Optik **156**, 459 (2018).

[73] M. Grinberg, *Opt. Mater.* **19**, 37 (2002).

[74] Z. Pan, Y. Y. Lu, F. Liu, Nat. Mater. **11**, 58 (2012).

[75] W. Y. Tian, K. X. Song, F. F. Zhang, P. Zheng, J. X. Deng, J. Jiang, J. M. Xu, H. B. Qin, J. Alloys Compd. **638**, 249 (2015).

[76] Z. C. Wu, Z. M. Zhang, C. Huang, J. Liu, M. M. Wu, Z. G. Xia, J. Alloys Compd. **734**, 43 (2018).

[77] R. Alcala, D. K. Sardar, W. A. Sibley, J. Lumin. **27**, 273 (1982).

[78] H.Q. Su, Z.H. Jia, C.S. Shi, J. Xin, S.A. Reid, Chem. Phys. Lett. **335**, 17 (2001).

[79] B. Latourrette, F. Guillen, C. Fouassier, Mater. Res. Bull. **14**, 865 (1979).

[80] L. Yang, Y.P. Wan, Y.L. Huang, X.G. Wang, H. Cheng, H.J. Seo, Mater Lett. **172**, 23 (2016).

[81]H. Terraschke, J. Olchowka, E. Geringer, A. V. Rodrigues, C. Wickleder, Small **1**, 1703707 (2018).

[82] R. J. Xie, N. Hirosaki, Appl. Phys. Lett. **84**, 5404 (2004).

[83] J. Y. Chen, N. M. Zhang, C. F. Guo, F. J. Pan, X. J. Zhou, H. Suo, X. Q. Zhao, E. M. Goldys, ACS Appl. Mater. Inter. **8**, 20856 (2016).

[84] D. Wang, Q. R. Yin, Y. X. Lia, M. Q. Wang, J Lumin. **97**, 1 (2002).

[85] M. P. Saradhi, U. V. Varadaraju, Chem. Mater. **18**, 5267 (2006).

[86] Z. G. Xia, H. K. Li, X. Li, C. Y. Liu, Dalton Trans. **42**, 16588 (2013).

[87] Y.L. Huang, S.Y. Zhang, S.I. Kim, Y.M. Yu, H.J. Seo, J. Electrochem. Soc. **159**, J23 (2011).

[88] C. Y. Xu, Y. D. Li, Y. L. Huang, Y. M. Yu, H. J. Seo, J. Mater. Chem. **22**, 5419 (2012).

[89] J. Y. Han, W. B. Im, G. Y. Lee, D. Y. Jeon, J. Mater. Chem. **22**, 8793 (2012).

[90] Z. G. Xia, H. K. Liu, X. Li, C. Y. Liu, Dalton Trans. **42**, 16588 (2013).

[91] M. Yu, J. Lin , J. Fang, Chem. Mater. **17**, 1783 (2005).

[92] D. D. Jia, J. Zhu, B. Q. Wu, J. Electrochem. Soc. **147**, 3948 (2000).

[93] Y. L. Huang, S. Y. Zhang, S. I. Kim, Y. M. Yu, H. J. Seo, J. Electrochem. Soc. **159** (2011) J23-J28

[94] S. Y. Zhang, Y. L. Huang, L. Shi, H. J. Seo, J. Phys-Condens. Mat. **22**,

235402 (2010).

[95] R. N. Hua, B. F. Lei, D. M. Xie, C. S. Shi, J. Solid State Chem. **175**, 284 (2003).

[96] R. G. Kunghatkar, S. J. Dhoble, P. S. Hemne. Lumin. **31**, 1503 (2016).

[97] C. Martineau, F. Fayon, M.R. Suchomel, M. Allix, D. Massiot, F. Taulelle, Inorg. Chem. **50**, 2644 (2011).

[98] P. P. Dai, S. P. Lee, T. S. Chan, C. H. Huang, Y. W. Chiang, T. M. Chen, J. Mater. Chem. C **4**, 1170 (2016).

[99] Z. G. Xia, X. M. Wang, Y. X. Wang, L. B. Liao, X. P. Jing, Inorg. Chem. **50**, 10134 (2011).

[100] J. Ni, Q. Liu, Z. Z. Zhou, G. H. Liu, RSC Adv. **7**, 42211 (2017).

[101] H. L. Yuan, Z. F. Huang, F. Chen, Q. Shen, L. M. Zhang, J. Alloys Compd. **720**, 521 (2017).

[102] J. Chen, Y. G. Liu, L. F. Mei, P. Peng, Q. J. Cheng, H. K. Liu, Sci. Rep. **6**, 31199 (2016).

[103] J. Zhou, Z. G. Xia, M. Y. Chen, M. S. Molokeev, Q. L. Liu, Sci. Rep. **5**, 12149 (2015).

[104] J. Chen, Y. G. Liu, L. F. Mei, H. K. Liu, M. H. Fang, Z. H. Huang, Sci. Rep. **5**, 9673 (2015).

[105] X. P. Fu, W. Lü, M. M. Jiao, H. P. You, Inorg. Chem. **55**, 6107 (2016).

[106] W. Z. Sun, Y. L. Jia, R. Pang, H. F. Li, T. F. Ma, D. Li, J. P. Fu, S. Zhang, L. H. Jiang, C. Y. Li, ACS Appl. mater. Inter. **7**, 25219 (2015).

[107] X. B. Qiao, H. J. Seo, J. Am. Ceram. Soc. **98**, 594 (2015).

[108] Y. L. Zhu, Y. J. Liang, S. Q. Liu, X. Y. Wu, R. Xu, K. Li, J. Alloys Compd. **698**, 49 (2017).

[109] C. S. Huang, C. L. Huang, Y. C. Liu, S. K. Lin, T. S. Chan, H. W. Tu, Chem. Mater. **30**, 1769 (2018).

[110] M. Y. Peng, X. W. Yin, P. A. Tanner, M. G. Brik, P. F. Li, Chem. Mater. **27**, 2938 (2015).

[111] Q. Zhou, Y. Y. Zhou, Y. Liu, L. J. Luo, Z. L. Wang, J. H. Peng, J. Yan, M. M. Wu, J. Mater. Chem. C. **3**, 3055 (2015).

[112] T. Murata, T. Tanoue, M. Iwasaki, K. Morinaga, T. Hase, J. Lumin. **114**, 207 (2005).

[113] K. Seki, K. Uematsu, K. Toda, M. Sato, Chem. Lett. **43**, 1213 (2014).

[114] M. A. Noginov, G. B. Loutts, J. Opt. Soc. Am. B. **16**, 3 (1999).

[115] G. B. Loutts, M. Warren, L. Taylor, R. R. Rakhimov, H. R. Ries, G. Miller, M. A. Noginov, M. Curley, N. Noginova, N. Kukhtarev, H. J. Caulfield, P. Venkateswarlu, Phys. Rev. B. **57**, 3706 (1998).

[116] Y. Zhydachevskii, D. Galanciak, S. Kobyakov, M. Berkowski, A. Kaminska, A. Suchocki, Y. Zakharko, A. Durygin, J. Phys. Condens. Matter. **18**, 11385 (2006).

[117] Y. Zhydachevskii, A. Durygin, A. Suchocki, A. Matkovskii, D. Sugak, P. Bilski, S. Warchol, Nucl. Instrum. Methods B **227**, 545 (2005).

[118] I. V. Kityk, M. Makowska-Janusik, M. D. Fontana, M. Aillerie, F. Abdi, J. Phys. Chem. B **105**, 12242 (2001).

[119] K. Hayashi, H. Noguchi, M. Ishii, Mater. Res. Bull. **21**, 401 (1986).

[120] U. Fano, Phys. Rev. **124**, 1866 (1961).

[121] G. Wang, Y. Huang, L. Zhang, Cryst. Growth. Des. **11**, 3895 (2011).

[122] S. A. Payne, L. L. Chase, H. W. Newkirk, IEEE. J. Quantum Electron. **24**, 2243 (1988).

[123] Y. J. Hsiao, C. W. Liu, B. T. Dai, Y. H. H. Chang. J. Alloys Compd. **475**, 698 (2009).

[124] Z. Y. Hou, P. P. Yang, C. X. Li, L. L. Wang, H. Z. Lian, Z. W. Quan, J. Lin, Chem. Mater. **20**, 6686 (2008).

[125] J. S. Zhong, W. Xu, Q. L. Chen, S. Yuan, Z. G. Ji, D. Q. Chen, Dalton T. **46**, 9959 (2017).

[126] Q. Y. Peng, R. P. Cao, Y. J. Ye, S. L. Guo, Z. F. Hu, T. Chen, G. T. Zheng, J. Alloys Compd. **725**, 139 (2017).

[127] J.H. Oh, Y.J. Eo, H.C. Yoon, Y.D. Huh, Y.R. Do, J. Mater. Chem. C **4** (2016) 8326-8348

[128] H. D. Nguyen, C. C. Lin, M. H. Fang, R. S. Liu, J. Mater. Chem. C. **2**, 10268 (2014).

[129] R.S. Liu, Phosphors, Springer, 2016.

[130] Z. W. Zhou, J. M. Zheng, R. Shi, N. M. Zhang, J. Y. Chen, R. Y. Zhang, H. Suo, E. M. Goldys, C. F. Guo, ACS. Appl. Mater. Intrer. **9**, 6177 (2017).

[131] S. Shigeo, M. William, Phosphor Handbook, CRC Press, Washington, DC (1998)

[132] M. Inokuti, F. Hirayama, J. Chem. Phys. **43**, 1978 (1956).

[133] L. Qin, D. L. Wei, Y. L. Huang, S. I. Kim, Y. M. Yu, H. J. Seo, J. Nanopart. Res. **15**, 1940 (2013).

[134] P. Q. Cai, L. Qin, C. L. Chen, J. Wang, H. J. Seo, Dalton T. **46**, 14331 (2017).

[135] A. Majchrowski, I. V. Kityk, E. Mandowska, A. Mandowski, J. Appl. Phys. **100**, 053101 (2006).

[136] T. Senden, F. T. H. Broers, A. Meijerink, Opt. Mater. **60**, 431 (2016).

[137] A. M. Srivastavaa, M. G. Brik, ECS. J. Solid. State. Soc. **7**, 3012 (2018).

[138] Z. Bryknar, V. Trepakov, Z. Potůček, L. Jastrabík, J. Lumin. **87**, 605 (2000).

[139] A. M. Srivastava, M. G. Brik, H. A. Comanzo, W. W. Beers, W. E.

Cohen, T. Pocock, ECS. J. Solid. State. Sci. Technol. **7**, 3158 (2018).

[140] M. G. Brik, A. M. Srivastava, J. Lumin. **133**, 69 (2013).

[141] M. G. Brik, S. J. Camardello, A. M. Srivastava, ECS. J. Solid. State. Sci. Technol. **4**, R39 (2015).

[142] B. Henderson, G. F. Imbusch, Optical Spectroscopy of Inorganic Solids, Clarendon Press, Oxford (1989).

[143] I. W. Forrest, A. P. Lane, Inorg. Chem. **15**, 265 (1976).

[144] Q. Y. Shao, H. Y. Lin, J. L. Hu, Y. Dong, J. Q. Jiang, J. Alloys Compd. **552**, 370 (2013).